On-chip electro-optic frequency shifters and beam splitters

https://doi.org/10.1038/s41586-021-03999-x

Received: 12 May 2020

Accepted: 7 September 2021

Published online: 24 November 2021



Check for updates

Yaowen Hu^{1,2}, Mengjie Yu¹, Di Zhu¹, Neil Sinclair^{1,3,4}, Amirhassan Shams-Ansari¹, Linbo Shao¹, Jeffrey Holzgrafe¹, Eric Puma¹, Mian Zhang⁵ & Marko Lončar^{1⊠}

Efficient frequency shifting and beam splitting are important for a wide range of applications, including atomic physics^{1,2}, microwave photonics³⁻⁶, optical communication^{7,8} and photonic quantum computing⁹⁻¹⁴. However, realizing gigahertz-scale frequency shifts with high efficiency, low loss and tunability-in particular using a miniature and scalable device—is challenging because it requires efficient and controllable nonlinear processes. Existing approaches based on acousto-optics^{6,15-17}, all-optical wave mixing^{10,13,18-22} and electro-optics²³⁻²⁷ are either limited to low efficiencies or frequencies, or are bulky. Furthermore, most approaches are not bi-directional, which renders them unsuitable for frequency beam splitters. Here we demonstrate electro-optic frequency shifters that are controlled using only continuous and single-tone microwaves. This is accomplished by engineering the density of states of, and coupling between, optical modes in ultralow-loss waveguides and resonators in lithium niobate nanophotonics²⁸. Our devices, consisting of two coupled ring-resonators, provide frequency shifts as high as 28 gigahertz with an on-chip conversion efficiency of approximately 90 per cent. Importantly, the devices can be reconfigured as tunable frequency-domain beam splitters. We also demonstrate a non-blocking and efficient swap of information between two frequency channels with one of the devices. Finally, we propose and demonstrate a scheme for cascaded frequency shifting that allows shifts of 119.2 gigahertz using a 29.8 gigahertz continuous and single-tone microwave signal. Our devices could become building blocks for future high-speed and large-scale classical information processors^{7,29} as well as emerging frequency-domain photonic quantum computers^{9,11,14}.

The progress of photonic science and technology is intimately related to the ability to utilize and precisely control all fundamental degrees of freedom of a photon. Although, for example, photon position (path) and polarization can be readily controlled using elementary optical components such as beam splitters and waveplates, frequency control is more challenging as it requires changing the energy of a photon. Typical approaches used for frequency control of light are based on acousto-optics, all-optical wave-mixing and electro-optics. Acousto-optic modulators use phonon scattering to control photon energy and can typically shift the frequency of light in the kHz to few GHz range^{15,16}. However, they have demonstrated high efficiency only in bulk structures that are not compatible with photonic integration. All-optical wave-mixing can achieve efficient frequency conversion in the THz range in bulk media 10,13,18 , and can be bi-directional 21,22 . However, it requires stringent phase matching conditions, can suffer from parasitic nonlinear processes, and is difficult to control due to a nonlinear dependence on optical power.

The electro-optic effect, utilized in modulators that are widely used in modern telecommunication networks, directly mixes microwave and optical fields and can be used to achieve frequency control of light. However, traditional electro-optic modulators inevitably produce undesired symmetric sidebands, and thus require filtering (for example, frequency or spatial), and are unable to achieve efficient frequency shifts. In-phase and quadrature (IQ) modulators eliminate symmetric sidebands via destructive interference among multiple modulators^{25,30,31}, which comes at the expense of a large fundamental upper-limit device loss of 4.7 dB and non-negligible higher-order sidebands. Serrodyne modulation, on the other hand, uses a saw-tooth waveform to generate frequency shifts²⁴, but extending this method to the GHz regime requires broadband and high-power electronics, which ultimately limits its practical usage. Other methods such as adiabatic tuning of the optical cavity resonance 23 or spectral shearing 26,32 , which applies a linear temporal phase to light with sinusoidal modulation, are capable of frequency shifting, but they require pulsed operation

1 John A. Paulson School of Engineering and Applied Sciences, Harvard University, Cambridge, MA, USA. 2 Department of Physics, Harvard University, Cambridge, MA, USA. 3 Division of Physics, Mathematics and Astronomy, California Institute of Technology, Pasadena, CA, USA. 4Alliance for Quantum Technologies (AQT), Pasadena, CA, USA. 5HyperLight Corporation, Cambridge, MA, USA. [⊠]e-mail: loncar@seas.harvard.edu

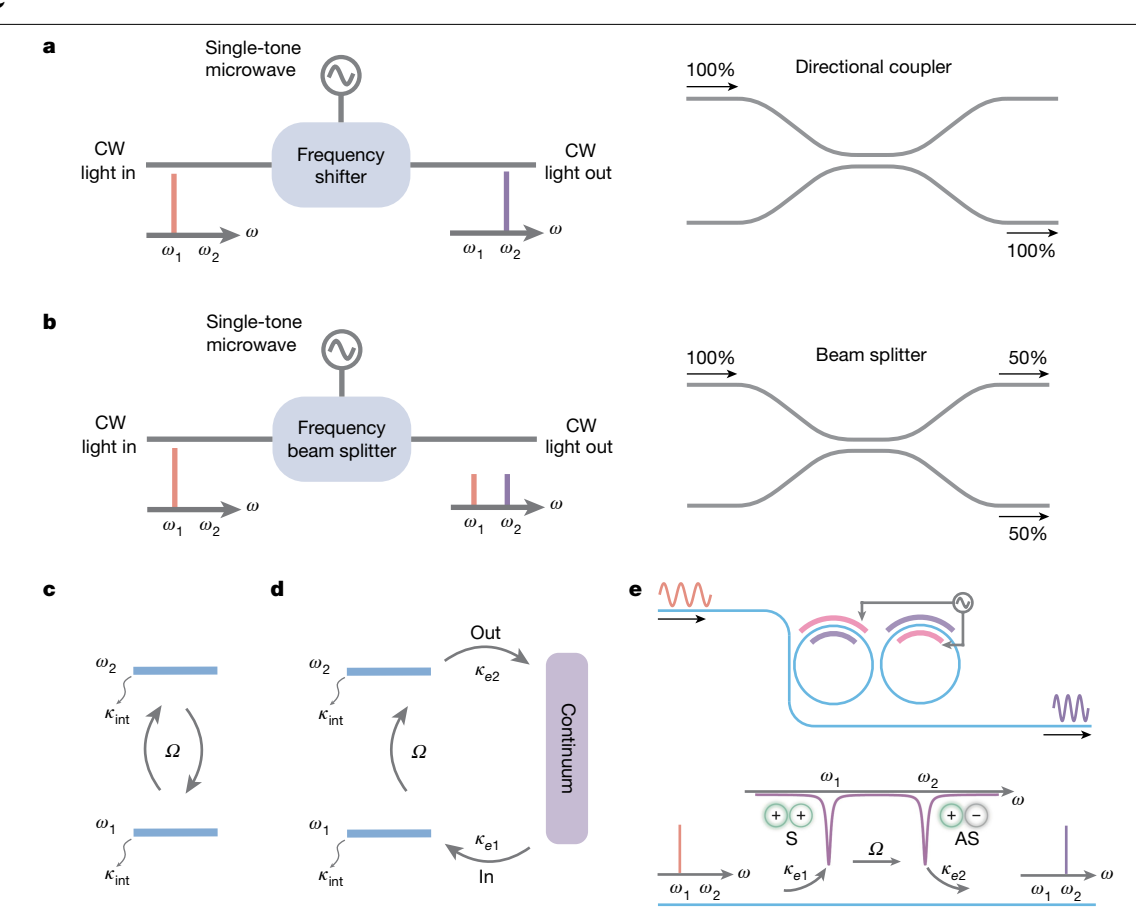


Fig. 1| **Concept of the electro-optic frequency shifter and beam splitter. a**, A frequency shifter converts light from one frequency to another, analogous to a directional coupler that changes the path (spatial modes) of a photon. **b**, A frequency beam splitter partially converts light from one frequency to another, similar to its spatial-mode counterpart. **c**, **d**, Principle of a GCC condition that allows complete transfer of energy between levels vis-a-vis frequency shifting of light. **c**, A coherent coupling Ω causes oscillation of energy between two discrete levels ω_1 and ω_2 (for example, two cavity modes), each has a decay rate of κ_{int} . **d**, Frequency shifting by coupling two discrete levels to a continuum. Light is coupled from the continuum to level ω_1 at a rate

 $\kappa_{\rm el}$, from level ω_1 to level ω_2 at a rate Ω , and from level ω_2 to the continuum at a rate $\kappa_{\rm e2}$. The GCC condition $\kappa_{\rm el} = \Omega = \kappa_{\rm e2} \gg \kappa_{\rm int}$ results in an efficient flow of energy. Note that the direction of energy flow is determined by which level is populated first, and transitions indicated by the coupling rates $\kappa_{\rm el}$, $\kappa_{\rm e2}$ and Ω are bi-directional in nature. **e**, Schematic of the device used to implement the GCC condition (top), and its frequency-domain representation (bottom). The coupled-ring system provides a pair of hybrid modes, referred to as symmetric (S) and anti-symmetric (AS). Coupling between them is induced by electro-optic modulation. CW, continuous wave.

with a known timing reference. Single sideband modulation using TE and TM modes of a high-quality factor (*Q*) whispering gallery mode toroid resonator has been demonstrated, albeit with limited efficiency and bandwidth (MHz level)²⁷. Consequently, a practical and efficient electro-optic device that can shift the frequency of light on demand is still missing. The situation is even more challenging when it comes to the realization of a tunable frequency beam splitter. Such a device, like its spatial counterpart, needs to be bi-directional, capable of frequency up- and down-shifting simultaneously or coherent mixing of two input channels without changing the configuration of the device or driving signal, and without affecting other degrees of freedom such as polarization or spatial modes. Based on these criteria, electro-optic frequency shifters based on in-phase and quadrature (IQ) modulators, the serrodyne method, adiabatic tuning and spectral shearing cannot act as frequency beam splitters.

Here we overcome these limitations and demonstrate on-chip electro-optic frequency shifters that have up to ~90% conversion efficiency, high carrier suppression ratio and low on-chip loss. Importantly, this is accomplished using only a single monotone and continuous microwave source. Our electro-optic frequency shifters act only on selected frequency modes without affecting other frequencies of light. Furthermore, they feature a tunable ratio between the optical power

at the shifted and pump frequency that is controlled by the applied microwave power. At the regime of full conversion, the frequency of all inserted photons is shifted to another frequency. In this regime the devices are analogous to a directional coupler (Fig. 1a): they swap two modes, but in the frequency rather than the spatial domain. On the other hand, in the regime of equal optical power between the light at shifted and pump frequency, the devices serve as a 50:50 frequency-domain beam splitter (Fig. 1b). By changing the power of the microwave signal, the splitting ratio can be controlled, and tunable frequency domain beam splitters can be realized. These operations (frequency shifting and beam splitting) represent the fundamental functionalities required for controlling the frequency degree of freedom of a photon, in analogy with the control of its polarization and path.

To realize the frequency shifting functionality, we introduce a general method to control the flow of light in the frequency domain. Consider two discrete photonic energy levels (Fig. 1c), which could be two resonances of an optical cavity or a doublet formed by a mode anti-crossing. When driven—for example, using coherent microwave signals and the electro-optic effect considered in this work—the two levels are coupled with a coupling rate of Ω , resulting in Rabi oscillation. As a result, the frequency of light inside such a system oscillates between two levels. To enable an efficient frequency shift, we introduce a continuum of

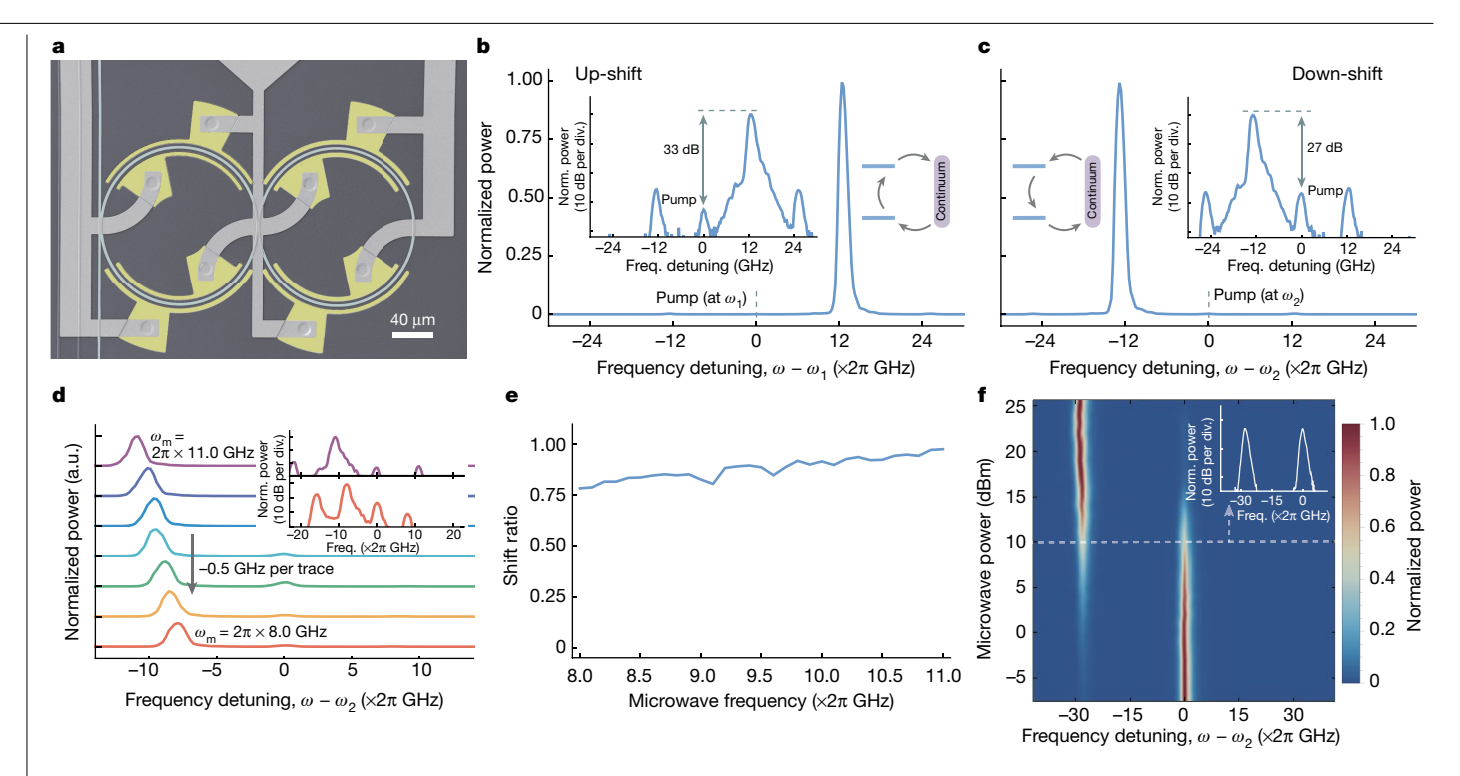


Fig. 2 | Electro-optic frequency shifter and beam splitter. a, Scanning electron microscopy (SEM) micrograph in false colour of a frequency shifting device with 28.2-GHz doublet splitting. The light blue represents the optical waveguide and ring resonators. Metal electrodes have two layers, connected by vias through the cladding oxide. Top and bottom electrode layers are represented by light grey and yellow, respectively. The electrodes are designed to minimize parasitic capacitance and inductance to achieve efficient modulation at high microwave frequencies. b, c, Electro-optic frequency shifter. Up-shifts (b) and down-shifts (c) of 12.5 GHz with 80% conversion efficiency and > 0.99 shift ratio (defined in text) at telecommunication wavelengths. The insets show the directions of energy flow using the

energy-level description of Fig. 1d and the spectra in dB scale. d, Frequency shift with microwave detuning. The shift ratio is reduced as the microwave frequency is detuned from 11 GHz (equal to the doublet splitting) to 8 GHz. The inset shows the spectra in dB scale when using 11-GHz (top part, purple trace) and 8-GHz (bottom, red trace) microwaves. e, Shift ratio for varied microwave $detuning. \textbf{\textit{f}}, Tunable frequency beam splitter. Increasing the microwave power and the property of the p$ changes the shift ratio continuously from 0 to near unity (0.987) at a shift-frequency of 28.2 GHz, allowing for a frequency beam splitter with a tunable splitting ratio. Inset, output optical spectrum in dB scale at 50:50 splitting under a microwave power of 10 mW. div., division.

levels (for example, optical waveguide) that couples to both discrete levels. Importantly, by controlling the coupling rates between different levels, the photons can be injected at one discrete level and extracted from the other one (Fig. 1d). Photons of frequency ω_1 are coupled from the continuum into level ω_1 with a rate of $\kappa_{\rm el}$, while being coupled out of level ω_2 back to the continuum with a rate $\kappa_{\rm e2}$. Assuming that each of the levels has a negligible intrinsic loss rate $\kappa_{int} \ll \kappa_{el}$, κ_{e2} , complete energy transfer (100% frequency shift) occurs when these three rates of energy exchange are balanced: $\kappa_{e1} = \Omega = \kappa_{e2}$ (see Methods for a detailed discussion on this condition). We refer to this as a generalized critical coupling (GCC) condition. Otherwise, when the condition is not met, partial energy transfer occurs between the two levels, and some fraction of the photons at frequency ω_1 are coupled back into the continuum. This is used to realize a tunable frequency domain beam splitter. Notably, when the GCC condition is satisfied, the reverse frequency conversion process will also be in a balanced state: photons injected from the continuum at frequency ω_2 will be converted to photons of frequency ω_1 and outcoupled to the continuum at that frequency.

We experimentally implement the proposed scheme using a device consisting of two coupled ring resonators (referred to as a two-resonator device) on thin-film lithium niobate (Fig. 1e), in which coherent coupling of two optical frequency modes is achieved via the electro-optic effect and microwave driving³³. Evanescent coupling between the two identical resonators gives rise to a resonance doublet which corresponds to symmetric (S) and anti-symmetric (AS) modes with frequencies ω_1 and ω_2 . A single bus waveguide provides a continuum of modes as well as the input and output ports of our device.

The two cavities are efficiently modulated using a single sinusoidal microwave drive (Fig. 1e, top), and support high frequencies owing to the small capacitance and parasitic inductance of the electrodes (Fig. 2a and Methods). Microwave driving induces a coherent coupling Ω between the S and AS modes, which is proportional to the peak voltage of the applied microwave signal. The doublet splitting (frequency differences between S and AS modes) is $2|\mu|$, where μ represents the coupling strength between coupled rings in the absence of a microwave drive. The microwave frequency $\omega_{\rm m}$ is matched to or detuned from the doublet splitting $2|\mu|$, depending on the experiment performed. The two rings are strongly coupled through evanescent coupling, and therefore can be considered as a single device. As a result, the S and AS modes can be accessed using a single waveguide placed in the proximity of one ring only. Furthermore, the coupling rate y between the waveguide and the left cavity (in Fig. 1e and 2a) is up to 31 times higher than the intrinsic loss κ_{int} of the cavity, yielding two strongly over-coupled modes with balanced effective mode–waveguide couplings of $\kappa_{\rm el} = \kappa_{\rm e2} = \gamma/2$ that satisfy the GCC condition (see Methods). Specifically, we fabricate devices with various doublet splittings of 11.0, 12.5 and 28.2 GHz at telecommunication wavelengths by changing the gap between the coupled rings.

We first demonstrate the frequency shifting feature of our two-resonator device, here continuous-wave light of frequency ω_1 (wavelength of 1,601.2 nm) and a microwave tone of frequency 12.5 GHz, which matches the splitting of the resonance doublet, are sent to the device. The output optical spectrum (Fig. 2b) shows that nearly all the power at frequency ω_1 (S mode) is converted to frequency ω_2 (AS mode),

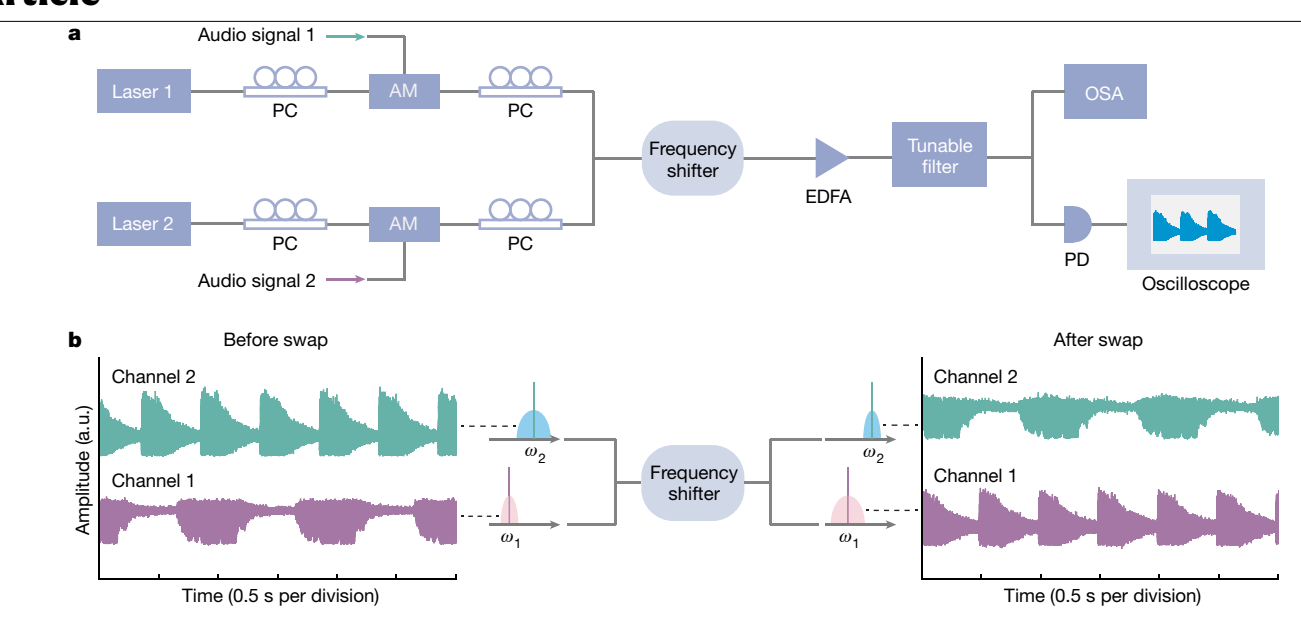


Fig. 3 | **Information swapping between two frequency channels. a**, Experimental set-up. Lasers 1 and 2 emit light of frequencies ω_1 and ω_2 , respectively, with 11 GHz detuning. The two beams are independently modulated to carry unique audio signals, combined, and then sent to the frequency shifter. The output optical spectrum is monitored by an optical spectrum analyser, and a tunable filter is used to select each frequency

channel. The time-domain signals are measured using a photodetector followed by a real-time oscilloscope. AM, amplitude modulator; EDFA, erbium-doped fibre amplifier; OSA, optical spectrum analyser; PC, polarization controller; PD, photodetector. $\bf b$, Time-domain audio signal in each channel before and after the swapping. The purple and green traces represent the audio signal in channel 1 (ω_1) and channel 2 (ω_2), respectively.

with a measured conversion efficiency of $\eta = 80\%$, and large carrier suppression ratio (CSR) of 33 dB. The conversion efficiency is defined as the ratio of the output power at the shifted frequency and the total input power inside the bus waveguide: $\eta = P_{\text{shift}}/P_{\text{in}}$ and the CSR is defined as the ratio of the output power at the shifted frequency and the pump frequency: $CSR = P_{shift}/P_{pump}$. Importantly, our device also operates in reverse; pumping at frequency ω_2 (AS mode) leads to a down-shift to frequency ω_1 with a measured $\eta = 80\%$ and a CSR of 27 dB (Fig. 2c). The device has a low on-chip loss α of only 0.92 dB (see Methods), defined as $\alpha = P_{out}/P_{in}$ (or $\alpha = -10\log_{10}(P_{out}/P_{in})$ in dB) in which P_{out} is the output power inside the bus waveguide. The fibre-to-chip facet loss is currently approximately 5-10 dB per facet. Spot-size converters³⁴ and adiabatic couplers³⁵ could be used to reduce this facet loss to below 1.7 dB per facet and 1.1 dB per facet, respectively. We also define shift ratio as $\epsilon = P_{\text{shift}}/P_{\text{out}}$, which we measure to be 0.994 and 0.993 for up- and down-shifts (Fig. 2b, c), respectively. We note that the conversion efficiency η can be decomposed as $\eta = \alpha \times \epsilon$, in which α and ϵ can be adjusted independently by varying different device parameters (see Methods). The microwave power used to achieve the up- and down-conversion (Fig. 2b, c) is 102 mW.

Second, we show that frequency shifts over a large microwave bandwidth can be achieved by tuning the microwave frequency. Light is injected into the AS mode (at frequency ω_2) of a device with an 11.0-GHz doublet splitting to realize a frequency down-shift. The microwave power is kept at 228 mW as we vary the microwave frequency from 11.0 GHz to 8.0 GHz. Accordingly, ϵ reduces from 0.977 to 0.784, indicating a 3-dB bandwidth of >3 GHz that is currently limited by the bandwidth of our microwave amplifier (Fig. 2d, e). The bandwidth of the shifter benefits from the strong over-coupling regime and large microwave modulation, yielding a bandwidth that is larger than the unmodulated cavity linewidth (see Methods). The shift ratio for different microwave detunings can be further optimized by varying the microwave power. In addition, the microwave operating frequency can be controlled by applying a d.c. voltage. For example, we experimentally (theoretically) show that the device with 12.5 GHz doublet splitting can be tuned to 16 GHz (>23 GHz) while maintaining a shift ratio ϵ = 0.991 (>0.9) (See Extended Data Fig. 6 and Methods). It is worth mentioning that our devices can operate without a typical conversion efficiency—bandwidth trade-off (see Methods). Another unique feature of our approach is that increasing the doublet splitting for larger frequency shifts does not degrade η , α , ϵ or the CSR, as long as the GCC condition is satisfied. This is experimentally confirmed using a 28.2-GHz device with measured η = 89%, CSR = 20 dB, α = 0.45 dB and ϵ = 0.987, using a 316-mW microwave driving power (Fig. 2f).

Next, we configure the 28.2-GHz device into a frequency beam splitter with a fully tunable power splitting ratio by varying the power of the microwave signal. As the microwave power is increased from 0.063 mW to 316 mW, the shift ratio ϵ (as well as the conversion efficiency η) of a down-shift continuously increases from 0 to near unity (Fig. 2f). At 10 mW microwave power, the optical power is split equally between the two frequency modes ω_1 and ω_2 , yielding a 50:50 frequency beam splitter (as illustrated in Fig. 1b and with results shown in the inset of Fig. 2f in dB scale). It should be noted that the frequency splitter, which is based on coherent mixing of optical and microwave fields 11.36, performs unitary operations (in the limit of vanishingly small loss) identical to a standard four-port configuration of a tunable spatial-mode beam splitter (see Methods).

To show that our two-resonator device can perform up- and down-shifts simultaneously (bi-directionality of a frequency beam splitter), we demonstrate information swapping between two frequencies using a single device, mimicking a four-port coupler (as depicted in Fig. 1a). Such an operation allows the exchange of information between frequency channels without detection, which is relevant to optical and quantum information processing. Here, two laser beams of frequency ω_1 and ω_2 are separately modulated by two different audio signals (Fig. 3a). The audio modulation labels the two frequencies, thereby distinguishing the shifted and residual signals after the swapping. The two laser beams are then combined and sent into our device. The measured audio signals of each channel at the output confirms the swap operation was performed (Fig. 3b). Discussion and results regarding modulation bandwidth, shifting of pseudorandom bit sequences and crosstalk are in Methods.

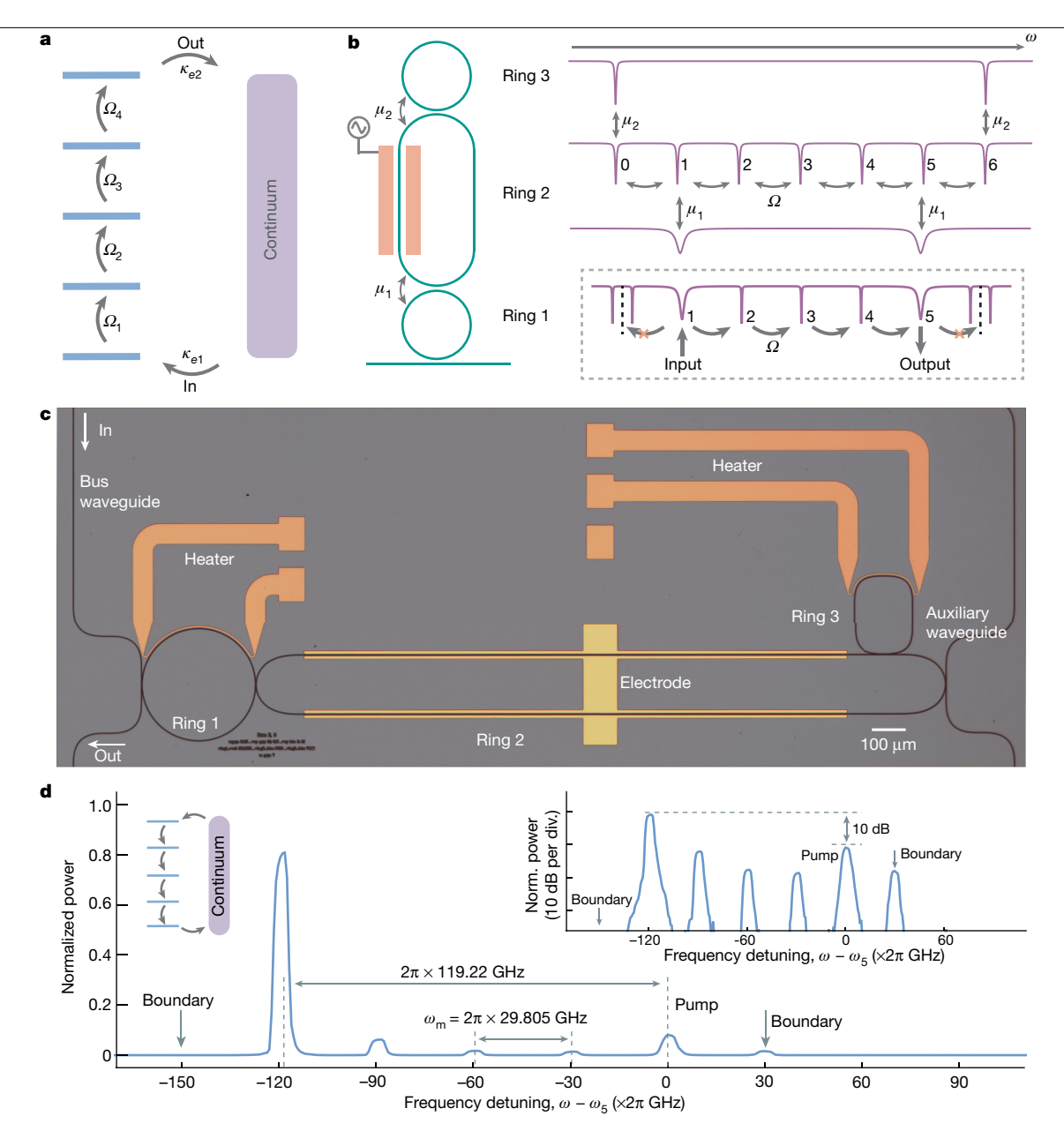


Fig. 4 | Cascaded frequency shifting. a, Balancing of coupling rates between several energy levels $\kappa_{e1} = \Omega_1 = \Omega_2 = \dots = \kappa_{e2}$ can permit efficient energy flow. b, Proposed structure to realize cascaded frequency shifting. It consists of three coupled rings: ring 2 provides a set of equally detuned energy levels, with a mode coupling rate of Ω induced by microwave modulation; ring 1 over-couples modes 1 and 5 to the waveguide; and ring 3 induces a boundary to the cascade process by mode splitting, μ_1 , coupling rate between ring 1 and 2; μ_2 , coupling rate between ring 2 and 3. The transmission spectrum of each ring is shown on the right, with the bottom-most panel that illustrates the energy flow of the device when pumping mode 1 under the GCC condition. \boldsymbol{c} , Device optical image (false colour). Three resonators, a small ring (ring 1), a racetrack

(ring 2) and rectangular-shaped (ring 3) resonator, are evanescently coupled to form a single device. The resonance frequencies of rings 1 and 3 are adjusted $using \ resistive \ heaters. \ A \ bus \ waveguide \ coupled \ to \ ring \ 1 \ provides \ the \ input$ and output ports as well as serving as the continuum. A weakly coupled auxiliary waveguide is used to monitor the resonances of rings 2 and 3 during the tuning process. **d**. Output spectrum of the cascaded frequency shifter. Continuous-wave light of 1,628.5 nm wavelength (corresponding to zero detuning), resonant with rings 1 and 2, is directed to the device. A continuous and single-tone microwave signal of $\omega_{\rm m} = 2\pi \times 29.805$ GHz is applied to the electrode, resulting in a four-mode cascaded frequency down-shift of 119.22 GHz.

We now show that our concept can be generalized to shift optical frequencies beyond 100 GHz. Although this can be achieved using two-resonator devices by further increasing the evanescent coupling between the resonators for a larger doublet splitting, this approach would require very high-frequency microwave electronics. To mitigate this, we propose a generalized 'cascaded' shifter by extending our scheme to a system consisting of multiple discrete levels coupled to a continuum (Fig. 4a). When coherent coupling between nearest-neighbour energy levels satisfies the GCC condition κ_{e1} =

 $\Omega_1 = \Omega_2 = \dots = \kappa_{e2}$, energy can efficiently flow from the input to output mode. As a result, a complete frequency shift can be achieved. A system that can realize this process is depicted in Fig. 4b, comprised of only three resonators and a single bus waveguide. A large microresonator (ring 2) provides a family of discrete modes separated by the free spectral range (FSR; for example, 30 GHz). Modulating this resonator at a frequency equal to the FSR provides coherent coupling between nearest-neighbour frequency modes^{36,37}. A small microresonator (ring 1) with a large FSR (for example, 120 GHz) is used to over-couple

two modes (for example, mode 1 and mode 5 in Fig. 4b) of ring 2 to the bus waveguide. Another microresonator (ring 3, FSR = 180 GHz) induces mode crossing and thus breaks the cascade process in ring 2 (that is, provides a boundary) since the modulation no longer couples the resultant doublet levels with their nearest-neighbour levels. Therefore, the number of modes n of the device is determined by the size of ring 1 and ring 3. A d.c. voltage or thermal tuning can be used to tune the resonances of all rings.

Finally, we demonstrate a cascaded frequency shifter using a device consisting of three mutually coupled resonators (Fig. 4c): a small ring resonator (ring 1) is used for coupling to the selected mode of the racetrack resonator (ring 2), and a rectangular-shaped resonator (ring 3) provides a frequency boundary. Telecommunication wavelength light resonant with rings 1 and 2 is directed to the device using a waveguide adjacent to ring 1. The waveguide serves as the continuum of modes. A 29.805-GHz microwave tone is applied to ring 2 (racetrack), matching its FSR. This results in a four-mode cascade and a frequency down-shift of 119.22 GHz, equal to the FSR of ring 1, owing to the boundary created by a ring 3. The output optical spectrum (Fig. 4d) reveals $\eta = 19\%$, CSR = 10 dB, ϵ = 0.809 and α = 6.17 dB, corresponding to 1.54 dB per mode in a four-step cascade. Improving the conversion efficiency, on-chip loss and the shift ratio can be achieved by reducing the coupling strengths μ_1 and μ_2 , which currently distort the FSR of the racetrack resonator through a non-resonant perturbation, leading to a non-ideal matching of the GCC condition (see Methods). A full set of parameters inferred from this device is outlined in Methods.

In summary, we proposed and demonstrated integrated, efficient and low-on-chip-loss electro-optic two-resonator frequency shifters and frequency beam splitters operating at tens of GHz frequency, as well as a cascaded frequency shifter that yields >100-GHz frequency shifts using microwave signals of tens of GHz. Our work is enabled by integrated lithium niobate photonics^{28,33,38}. Compared to our previous work on a photonic molecule that required pulsed optical and microwave inputs, and precise timing between the two (to interrupt the Rabi oscillation cycle)³³, our current approach leverages precisely engineered couplings among discrete and a continuum of optical modes. Therefore, complete control of the energy flow in the frequency domain can be achieved using only simple sinusoidal continuous-wave microwave signals. This enables frequency shifting and beam-splitting of both pulsed and continuous-wave optical signals, without any synchronization requirements, as well as a wide operating bandwidth owing to the strongly over-coupled operating regime. Furthermore, our approach extends to a multi-level system, which leads to the realization of a cascaded frequency shifter. Improvements to the optical intrinsic Q and the use of a microwave cavity can further reduce the on-chip loss and drive voltage of the devices, respectively. For example, increasing the optical intrinsic Q to 10^7 (ref. ²⁸) will reduce the on-chip loss of the two-resonator device to 0.04 dB, or can reduce both the on-chip loss and drive voltage to 0.2 dB and 1 V, respectively (see Methods). Notably, dynamic control of the shifted light can be achieved by replacing the coupling gap with a microwave-driven Mach–Zehnder interferometer³⁹ and by applying broadband microwave signals. The ability to process information in the frequency domain in an efficient, compact and scalable fashion has the potential to greatly reduce the resource requirements for cascaded and large-scale photonic circuits, for example, for linear optical $quantum \, computing^{11,12} \, and \, multiplexed \, quantum \, communication^{40}.$ Efficient and on-demand shifting of light may also allow for control of the emission spectrum of solid-state single-photon emitters to create indistinguishable single photons or to produce deterministic single photons from probabilistic emitters^{41,42}. Our reconfigurable frequency shifter could become a fundamental building block for frequency-encoded information processing that offers benefits to telecommunications⁷, radar⁴³, optical signal processing²⁹, spectroscopy44 and laser control45.

Online content

Any methods, additional references. Nature Research reporting summaries, source data, extended data, supplementary information, acknowledgements, peer review information; details of author contributions and competing interests; and statements of data and code availability are available at https://doi.org/10.1038/s41586-021-03999-x.

- Greiner, M., Mandel, O., Esslinger, T., Hänsch, T. W. & Bloch, I. Quantum phase transition from a superfluid to a Mott insulator in a gas of ultracold atoms. Nature 415, 39-44 (2002).
- Hu, J. et al. Creation of a Bose-condensed gas of ⁸⁷Rb by laser cooling. Science. **358**, 1078-1080 (2017).
- Supradeepa, V. R. et al. Comb-based radiofrequency photonic filters with rapid tunability and high selectivity, Nat. Photon, 6, 186-194 (2012)
- Marpaung, D., Yao, J. & Capmany, J. Integrated microwave photonics. Nat. Photon. 13, 80-90 (2019).
- Fandiño, J. S., Muñoz, P., Doménech, D. & Capmany, J. A monolithic integrated photonic microwave filter. Nat. Photon. 11, 124-129 (2016).
- Eggleton, B. J., Poulton, C. G., Rakich, P. T., Steel, M. J. & Bahl, G. Brillouin integrated photonics, Nat. Photon, 13, 664-677 (2019).
- Yoo, S. J. B. Wavelength conversion technologies for WDM network applications. J. Light. Technol. 14, 955-966 (1996).
- Lukens, J. M. et al. All-optical frequency processor for networking applications. J. Light. Technol. 38, 1678-1687 (2020).
- Kues, M. et al. On-chip generation of high-dimensional entangled quantum states and their coherent control. Nature 546, 622-626 (2017).
- Kobayashi, T. et al. Frequency-domain Hong-Ou-Mandel interference. Nat. Photon. 10, 441-444 (2016)
- Lukens, J. M. & Lougovski, P. Frequency-encoded photonic qubits for scalable quantum information processing. Optica 4, 8-16 (2016).
- Lu, H. H. et al. Electro-optic frequency beam splitters and tritters for high-fidelity photonic quantum information processing. Phys. Rev. Lett. 120, 30502 (2018).
- Joshi, C. et al. Frequency-domain quantum interference with correlated photons from an integrated microresonator. Phys. Rev. Lett. 124, 143601 (2020)
- Kues, M. et al. Quantum optical microcombs. Nat. Photon. 13, 170-179 (2019).
- Kittlaus, E. A., Otterstrom, N. T., Kharel, P., Gertler, S. & Rakich, P. T. Non-reciprocal interband Brillouin modulation, Nat. Photon, 12, 613-619 (2018)
- Sohn, D. B., Kim, S. & Bahl, G. Time-reversal symmetry breaking with acoustic pumping of nanophotonic circuits, Nat. Photon, 12, 91-97 (2018).
- Liu, Q., Li, H. & Li, M. Electromechanical Brillouin scattering in integrated optomechanical waveguides. Optica 6, 778-785 (2019).
- Huang, J. & Kumar, P. Observation of quantum frequency conversion. Phys. Rev. Lett. 68, 2153-2156 (1992).
- Li, Q., Davanco, M. & Sriniyasan, K. Efficient and low-noise single-photon-level frequency conversion interfaces using silicon nanophotonics. Nat. Photon. 10, 406-414 (2016)
- Heuck, M. et al. Unidirectional frequency conversion in microring resonators for on-chip frequency-multiplexed single-photon sources. New J. Phys. 21, 33037 (2019).
- Raymer, M. G., van Enk, S. J., McKinstrie, C. J. & McGuinness, H. J. Interference of two photons of different colour. Opt. Commun. 283, 747-752 (2010).
- Pelc, J. S. et al. Dual-channel, single-photon upconversion detector at 13 µm. Opt. Express 20, 19075-19087 (2012).
- Preble, S. F., Xu, Q. & Lipson, M. Changing the colour of light in a silicon resonator. Nat. Photon. 1, 293-296 (2007).
- Johnson, L. M. & Cox, C. H. Serrodyne optical frequency translation with high sideband suppression. J. Light. Technol. 6, 109-112 (1988).
- Izutsu, M., Shikama, S. & Sueta, T. Integrated optical SSB modulator/frequency shifter. IEEE J. Quantum Electron. 17, 2225-2227 (1981).
- Wright, L. J., Karpiński, M., Söller, C. & Smith, B. J. Spectral shearing of quantum light pulses by electro-optic phase modulation. Phys. Rev. Lett. 118, 23601 (2017).
- Saychenkov, A. A. et al. Tunable optical single-sideband modulator with complete sideband suppression, Opt. Lett. 34, 1300-1302 (2009).
- Zhang, M., Wang, C., Cheng, R., Shams-Ansari, A. & Lončar, M. Monolithic ultra-high-Q lithium niobate microring resonator. Optica 4, 1536-1537 (2017).
- Frankel, M. Y. & Esman, R. D. Optical single-sideband suppressed-carrier modulator for wide-band signal processing. J. Light. Technol. 16, 859-863 (1998)
- Lo, H.-P. & Takesue, H. Precise tuning of single-photon frequency using an optical single
- sideband modulator, Optica 4, 919-923 (2017). Xu, M. et al. High-performance coherent optical modulators based on thin-film lithium
- niobate platform. Nat. Commun. 11, 3911 (2020). Fan, L. et al. Integrated optomechanical single-photon frequency shifter. Nat. Photon. 10,
- 766-770 (2016). Zhang, M. et al. Electronically programmable photonic molecule. Nat. Photon. 13, 36-40 (2019).
- He, L. et al. Low-loss fibre-to-chip interface for lithium niobate photonic integrated circuits. Opt. Lett. 44, 2314-2317 (2019).
- Khan, S. et al. Low-loss, high-bandwidth fibre-to-chip coupling using capped adiabatic tapered fibers, APL Photonics 5, 056101 (2020).
- Yuan, L., Lin, Q., Xiao, M. & Fan, S. Synthetic dimension in photonics. Optica 5, 1396-1405 (2018).
- Hu, Y., Reimer, C., Shams-Ansari, A., Zhang, M. & Loncar, M. Realization of high-dimensional frequency crystals in electro-optic microcombs. Optica 7, 1189-1194 (2020)

- Wang, C. et al. Integrated lithium niobate electro-optic modulators operating at CMOS-compatible voltages. Nature 562, 101-104 (2018).
- 39. Soltani, M. et al. Efficient quantum microwave-to-optical conversion using electro-optic nanophotonic coupled resonators. Phys. Rev. A 96, 043808 (2017).
- Sinclair, N. et al. Spectral multiplexing for scalable quantum photonics using an atomic frequency comb quantum memory and feed-forward control. Phys. Rev. Lett. 113, 053603
- 41. Joshi, C., Farsi, A., Clemmen, S., Ramelow, S. & Gaeta, A. L. Frequency multiplexing for quasi-deterministic heralded single-photon sources. Nat. Commun. 9, 847 (2018).
- Grimau Puigibert, M. et al. Heralded single photons based on spectral multiplexing and feed-forward control. Phys. Rev. Lett. 119, 083601 (2017).
- 43. Ghelfi, P. et al. A fully photonics-based coherent radar system. Nature 507, 341–345
- 44. Demtröder, W. Laser Spectroscopy. Volume 2: Experimental Techniques (Springer, 2008).
- Kohlhaas, R. et al. Robust laser frequency stabilization by serrodyne modulation. Opt. Lett. 37, 1005-1007 (2012).

 $\textbf{Publisher's note} \ \textbf{Springer Nature remains neutral with regard to jurisdictional claims in}$ published maps and institutional affiliations.

© The Author(s), under exclusive licence to Springer Nature Limited 2021

Methods

Device fabrication

Our two-resonator devices are fabricated from a commercial x-cut lithium niobate (LN) on insulator wafer (NANOLN), with a 600-nm LN layer, 2-µm buried oxide (thermally grown), on a 50-µm Si handle. Electron-beam lithography with hydrogen silsesquioxane (HSQ) resist followed by Ar⁺-based reactive ion etching (350-nm etch depth) is used to pattern the optical layer of the devices, including the rib waveguides and microresonators. The devices are cleaned, and microwave electrodes (15 nm of Ti, 300 nm of Au and 15 nm of Ti) are defined by photolithography followed by electron-beam evaporation and a bilayer lift-off process. These 'bottom electrodes' provide electric fields across each of the rings. Two layers of SiO_2 (0.8 µm + 0.8 µm) using plasma-enhanced chemical vapor deposition (PECVD) are used to clad the devices. Vias are subsequently patterned using photolithography and etched through the oxide using hydrofluoric acid. Finally, another layer of metal (15 nm of Ti and 500 nm of Au) is patterned by photolithography, electron-beam evaporation and lift-off. These 'top electrodes' are used to route microwave signals and deliver them to the bottom electrodes. The crossovers are needed to ensure the desired polarities for microwave modulation. In the case of the ~28-GHz two-resonator device (Fig. 2a), the shape of the top electrode is chosen to minimize its overlap with the bottom electrode, and thus minimize the parasitic capacitance formed between them. Furthermore, the top electrode is also narrow in order to reduce the parasitic capacitance formed between electrodes in that layer without affecting the microwave power handling capability. These design choices reduce the RC constant of the electrodes and allow for efficient modulation at high microwave frequencies. Lower frequency two-resonator devices, with 12.5-GHz and 11.0-GHz doublet splitting, use a top electrode structure akin to that in ref. 33. An illustration of the cross-section of the electrodeand resonator-regions of a two-resonator device is shown in Extended Data Fig. 1a. The inclined sidewall of vias (Extended Data Fig. 1a), owing to the wet-etch process, ensures that two layers of metal can make contact through electron-beam evaporation.

Our three-resonator devices (cascaded frequency shifters) are fabricated from an x-cut lithium niobate wafer (600-nm LN layer, 2- μ m buried oxide, 500- μ m Si handle). The optical layer (that is, the waveguides and microresonators) are defined using a similar approach as our two-resonator devices (electron-beam lithography and Ar $^+$ -based reactive ion etching with 350-nm etch depth and 800-nm SiO $_2$ cladding). The electrode for modulating ring 2 (15 nm of Ti and 300 nm of Au) is patterned by photolithography, electron-beam evaporation and a bilayer lift-off process. The heaters (15 nm of Ti and 200 nm Pt) for ring 1 and ring 3 are defined by photolithography followed by electron-beam evaporation and lift-off.

The heater is designed as a short metal strip (5 μ m width) that is placed 3 μ m away from the resonator on top of the SiO₂ cladding. The resistance of the heater is -140 Ω (including parasitic resistance from routing strips). Tuning of the ring resonance by the FSR is achieved with a current of -50 mA.

Frequency shifting characterization

The measurement set-up is illustrated in Extended Data Fig. 1b. Telecommunication-wavelength light from a fibre-coupled tunable laser (SANTEC TSL-510) passes through a polarization controller and is coupled to the LN chip using a lensed fibre. The output is collimated using an aspheric lens and then sent to an optical spectrum analyser (OSA) with a spectral resolution of 0.02 nm for characterization of the frequency shift. The microwave signal is generated from a synthesizer followed by a microwave amplifier. After passing through a circulator, the microwave signal is combined with a d.c. bias through a bias-tee and delivered to the electrodes on a device using an electrical probe. The d.c. signal tunes the optical resonances of both rings to achieve

a degenerate condition and form symmetric (S) and anti-symmetric (AS) hybrid modes. The frequency shifts for two-resonator devices with 12.5-GHz, 11.0-GHz and 28.2-GHz doublet splittings are measured at pump wavelengths of 1,601.3 nm, 1,631.5 nm and 1,633.2 nm, respectively. Heaters in the cascaded frequency shifter are driven using a d.c. bias (not shown in Extended Data Fig. 1b) and are used to tune the optical resonances of the small (ring 1) and rectangular-shaped (ring 3) rings of the cascaded shifter. In the measurements of two-resonator devices we use hundreds of microwatts of power in a bus waveguide, which translates to several milliwatts of power inside the rings, owing to the modest finesse of our strongly over-coupled cavities. Handling of optical powers as high as ~50 W have been demonstrated in LN ring resonators⁴⁶. However, with high optical powers, lithium niobate rings can suffer from resonance shifts, as well as drifts when a d.c. voltage is applied, owing to the photorefractive effect. This can be mitigated by doping or using feedback control. Alternatively, thermo-optic shifts induced by heaters can be used, as was demonstrated for the cascaded shifter. Moreover, our devices can maintain high performance under large frequency detuning of the resonances of each ring (see Extended Data Fig. 6 and Methods section 'Controlling the shift frequency with d.c. voltage applied to two-resonator devices'), which also helps reduce the negative effect of d.c. bias drift.

The main source of error in estimating the shift ratio ϵ is the imperfect polarization control of the input light. Each shifter is designed to operate using a transverse electric (TE) mode. Control of the purity of the input polarization is limited by the 20–30 dB extinction ratio of the polarization controller. In the experiment we verified the polarization of the output light on a two-resonator device with 11.0-GHz doublet splitting and found the unshifted pump power is predominantly in the transverse magnetic (TM) mode (see Extended Data Fig. 2). The TM mode is not efficiently shifted, leading to an underestimation of the optimal shift ratio.

$Optical \ and \ modulation \ bandwidths \ of the two-resonator \ devices$

Additional experiments were performed to verify the optical and modulation bandwidths of the two-resonator devices. The input laser beam is modulated using a commercial amplitude modulator driven by a vector network analyser (VNA). It passes through a device, undergoes a frequency up-shift and is sent back to the VNA (Extended Data Fig. 3a). The 3-dB modulation bandwidth of the frequency channel is 2.2 GHz. corresponding to a 4.4-GHz optical bandwidth (Extended Data Fig. 3b). We find that by increasing the microwave driving power of the shifter from 126 mW to 398 mW, the modulation bandwidth can be broadened to 4.1 GHz, which is due to the microwave-induced linewidth broadening effect discussed in the theoretical analysis in Methods. The electro-optic S_{21} for both microwave critical drive and over drive are normalized to that of the microwave critical-drive case at the lowest frequency (10 MHz), and the instrument responses (including amplitude modulator, photodetector and filter bandwidths) are calibrated. From the low-frequency electro-optic S_{21} , we found that the optical power loss is 1.15 dB, which is consistent with the on-chip loss (0.92 dB).

The frequency channel is also modulated by actual data streams to further demonstrate the device performance for GHz-scale channel bandwidths. We generate pseudorandom bit sequences at 1.000 Gbit s⁻¹ and 3.125 Gbit s⁻¹ using an arbitrary waveform generator (Extended Data Fig. 3a). Eye diagrams are measured to characterize the device performance (Extended Data Fig. 3c, d). The data rates that we used are currently limited by the sampling rate of the arbitrary waveform generator. By comparing the amplitude of the eye diagrams before and after up-shifts, we confirmed that the loss (-1 dB) is consistent with the measured 0.92-dB on-chip loss for the data in Fig. 2, and we did not observe added noise from our device. The eye diagrams before shift are measured by tuning the laser beam off-resonance and setting the centre of the filter window at the frequency of the laser beam.

For both before and after shift, the bandwidth of the filter is kept the same and the microwave driving powers are kept at 126 mW (the case of microwave critical drive in the modulation bandwidth measurement, Extended Data Fig. 3b).

The measurement of modulation bandwidth and channel shifting with pseudorandom bit sequences are both performed on the device with 12.5 GHz doublet splitting (Fig. 2b, c). The optical wavelength is set to 1,560.7 nm at which the doublet splitting changes to 11.3 GHz owing to optical dispersion.

In addition, to potentially suit some applications that require a higher bandwidth, we show that the optical bandwidth of a two-resonator device can be further improved by increasing the waveguide–cavity coupling γ . For example, improving the waveguide–cavity coupling γ to $2\pi\times20$ GHz leads to κ_e = $2\pi\times10$ GHz, whereas keeping the other parameters the same as for the current 28.2-GHz device ($\kappa_{\rm int}$ = $2\pi\times170$ MHz, $\omega_{\rm m}$ = $2\pi\times28.2$ GHz) would result in a 3-dB optical bandwidth of -14 GHz (simulation, Extended Data Fig. 4) with a driving microwave power of 1.35 W for a full frequency shift (238 mW for 50–50 split), a suppression of 26.7 dB on parasitic sidebands (see Methods section 'Limitation of the shift ratio of the two-resonator devices' for discussion on parasitic sidebands), and an on-chip loss of 0.13 dB.

Measurement of swap operation

An experimental demonstration of the swap operation is performed at a wavelength of 1,560.6 nm using a two-resonator device (set-up shown in Fig. 3a). We first set the frequency of two laser beams to be far detuned from the doublet resonance and measure the time-domain audio signals as references. This corresponds to the case in which the signals are not swapped. We then tune the frequency of each laser beam to be on resonance with one of the modes of a doublet, that is, laser 1(2) in S (AS) mode. In this case, frequency components of laser beam 1 are up-shifted and frequency components of laser beam 2 are down-shifted. The amplitudes of the time domain signal before and after swapping are renormalized for comparison in Fig. 3b.

Another measurement of the swap is performed to quantify the crosstalk of this operation using a two-resonator device (Extended Data Fig. 5). Laser beams 1 and 2 are, respectively, modulated by a sinusoidal signal as to define two frequency channels. The sinusoidal signal in channel 1 is swept from 200 MHz to 2.8 GHz, whereas the signal in channel 2 is fixed at 1 GHz (Extended Data Fig. 5a). The swap operation is then performed, the filter is tuned to pass first channel 1 and then channel 2, and the transmitted signals are detected by a photodiode followed by a real-time spectrum analyser. The radio frequency (RF) spectra are analysed to obtain the crosstalk, which is defined as the ratio between the shifted frequency and residual frequency. An example of the RF spectra when the modulation frequency in channel 1 is at 2.6 GHz (the modulation frequency in channel 2 is fixed at 1 GHz) are plotted. It shows that the spectrum is clean and the crosstalk is low in both channels (Extended Data Fig. 5b). The frequency component at 1.6 GHz in channel 1 is the beat note between the shifted (1 GHz) and residual frequency (2.6 GHz). The frequency at 2 GHz in channel 1 is the second harmonic signal generated by the amplitude modulator, which is verified before the swap measurement. By sweeping the modulation frequency of channel 1 from 200 MHz to 2.8 GHz, we find the crosstalk for both channels is low (approximately -35 dB) when the modulation frequency of channel 1 is at several hundreds of MHz and gradually increases to about -25 dB at 2.8 GHz (Extended Data Fig. 5c). The crosstalk is measured on the same device used for the modulation bandwidth measurement with the same optical wavelength and microwave driving power (126 mW, the case of microwave critical drive in the modulation bandwidth measurement, Extended Data Fig. 3b).

Note that simulations show the shift ratio ϵ of the swap measurement to be not overly sensitive to variations of the drive RF power. Specifically, changes in the microwave powers in the range of ~3 decibel milliwatts (dBm) vary the efficiency by no more than 5 per cent.

Numerical simulation of the two-resonator device

To numerically simulate the two-resonator device, we use a system of phase-modulated coupled cavities to demonstrate an efficient frequency shift. The Hamiltonian of this system can be described as

$$H = \omega_{\text{ring1}} a_1^{\dagger} a_1 + \omega_{\text{ring2}} a_2^{\dagger} a_2 + \mu (a_1^{\dagger} a_2 + a_1 a_2^{\dagger}) + \Omega \cos(\omega_{\text{m}} t + \varphi) (a_1^{\dagger} a_1 - a_2^{\dagger} a_2),$$

where a_1 and a_2 are the annihilation operators of the optical fields in cavities 1 and 2, whereas ω_{ring1} and ω_{ring2} are the corresponding cavity resonance frequencies, μ is the coupling strength between the two optical cavities due to the evanescent coupling, Ω is the modulation strength which is proportional to the microwave peak voltage, ω_{m} is the microwave frequency, and φ is the phase of the microwave signal. Here and henceforth $\hbar=1$. The minus sign in the last term is due to the modulation configuration of our system, in which the applied external voltage increases (decrease) the frequency of the resonance of ring 1 (2).

The equations of motion are based on the Heisenberg–Langevin equation derived from the Hamiltonian of the system. Accordingly, we obtain the equation of motion in the laser rotating frame:

$$\dot{a}_1 = \left(-\mathrm{i}(\omega_{\mathrm{ring1}} - \omega_{\mathrm{L}}) - \frac{\gamma + \kappa_{\mathrm{int}}}{2}\right) a_1 - \mathrm{i}\Omega \cos(\omega_{\mathrm{m}}t + \varphi) a_1 - \mathrm{i}\mu a_2 - \sqrt{\gamma} \alpha_{\mathrm{in}}$$

$$\dot{a}_2 = \left(-i(\omega_{\text{ring2}} - \omega_{\text{L}}) - \frac{\kappa_{\text{int}}}{2}\right)a_2 + i\Omega\cos(\omega_{\text{m}}t + \varphi)a_2 - i\mu a_1,$$

where γ is the waveguide–ring coupling and $\kappa_{\rm int}$ is the intrinsic loss of the ring. The amplitude of the input field is $\alpha_{\rm in} = \sqrt{P_{\rm in}/\omega_{\rm L}}$, and the input pump power and frequency are $P_{\rm in}$ and $\omega_{\rm L}$, respectively. The simulation is performed by numerically solving these equations of motion to obtain the output field amplitude as $a_{\rm out} = \alpha_{\rm in} + \sqrt{\gamma} a_{\rm L}$ In the end, a Fourier transform is performed to analyse the frequency component of the output field.

Theoretical analysis of the two-resonator device

The above equations can be solved analytically using several transformations and approximations. We consider the case that the two rings are identical, that is, $\omega_{\text{ring1}} = \omega_{\text{ring2}} = \omega_0$. Then the Hamiltonian can be transformed to the basis of symmetric (S) mode $c_1 = (a_1 + a_2)/\sqrt{2}$ and anti-symmetric (AS) mode $c_2 = (a_1 - a_2)/\sqrt{2}$ In this basis, the Hamiltonian of the system transforms to

$$H = \omega_1 c_1^{\dagger} c_1 + \omega_2 c_2^{\dagger} c_2 + \Omega \cos(\omega_m t + \varphi) (c_1^{\dagger} c_2 + \text{h.c.}),$$

where $\omega_1 = \omega_0 - \mu$ and $\omega_2 = \omega_0 - \mu$. As before, the equations of motion in the basic of c_1 , c_2 can be derived from the Heisenberg–Langevin equations, yielding:

$$\dot{c}_1 = \left(-i\omega_1 - \frac{\kappa_1}{2}\right)c_1 - i\Omega\cos(\omega_m t + \varphi)c_2 - \sqrt{\kappa_{e1}}\alpha_{in}e^{-i\omega_L t},$$

$$\dot{c}_2 = \left(-i\omega_2 - \frac{\kappa_2}{2}\right)c_2 - i\Omega\cos(\omega_m t + \varphi)c_1 - \sqrt{\kappa_{e2}}\alpha_{in}e^{-i\omega_L t},$$

where κ_{e1} and κ_{e2} are the external loss rate to the waveguide for the S and AS modes, κ_{int} is the intrinsic loss, $\kappa_j = \kappa_{ej} + \kappa_{\text{int}}$ is the total linewidth of the S (j=1) and AS (j=2) modes, ω_L and α_{in} is the frequency and amplitude of the input field. For our system, $\kappa_{e1} = \kappa_{e2} = \gamma/2$ because the S and AS modes physically occupy both rings, while only ring $1(\alpha_1)$ is coupled to the bus waveguide with a rate γ . For simplicity, we assume $\kappa_e = \kappa_{e1} = \kappa_{e2}$ and $\kappa = \kappa_1 = \kappa_2$.

With the symmetric mode being pumped, the modes c_1 , c_2 can be replaced by their slowly varying amplitudes as $c_1
ightharpoonup c_1 e^{-i\omega_L t}$ and

 $c_2 \rightarrow c_2 e^{-i\omega_L t} e^{-i\omega_n t}$. Under the rotating wave approximation, the equations of motion become

$$\dot{c}_1 = \left(i\Delta - \frac{\kappa}{2}\right)c_1 - i\frac{\Omega}{2}e^{i\varphi}c_2 - \sqrt{\kappa_e}\alpha_{in},$$

$$\dot{c}_2 = \left(i\Delta + i\delta - \frac{\kappa}{2}\right)c_2 - i\frac{\Omega}{2}e^{-i\varphi}c_1 - \sqrt{\kappa_e}\alpha_{in}e^{i\omega_{m}t},$$

where $\Delta = \omega_L - \omega_1$ is the laser detuning with respect to the S mode and $\delta = \omega_m - 2\mu$ is the detuning of microwave field with respect to the S-AS doublet splitting. Using the fact that c_2 is off-resonantly pumped, the pump term in the equation of motion of c_2 can be neglected, and the steady-state solution can be obtained (for simplicity, we set $\varphi = 0$):

$$c_1 = \frac{\sqrt{\kappa_e} \alpha_{\rm in}}{i\Delta - \frac{\kappa}{2} + \frac{\Omega^2/4}{i\Delta + i\delta - \frac{\kappa}{2}}},$$

$$c_2\!=\!i\frac{\varOmega}{2}\frac{\sqrt{\kappa_e}\alpha_{in}}{\left(i\!\varDelta-\!\frac{\kappa}{2}\right)\!\left(i\!\varDelta+i\!\delta-\!\frac{\kappa}{2}\right)+\frac{\varOmega^2}{4}}.$$

The output field will then be

$$a_{\text{out}} = \alpha_{\text{in}} e^{-i\omega_L t} + \sqrt{\kappa_e} (c_1 e^{-i\omega_L t} + c_2 e^{-i\omega_L t} e^{-i\omega_m t}).$$

The output field can be rewritten as two different frequency components $a_{\rm out}=A_0{\rm e}^{-{\rm i}\omega_L t}+A_+{\rm e}^{-{\rm i}\omega_L t}{\rm e}^{-{\rm i}\omega_n t}$ with $A_0=\alpha_{\rm in}+\sqrt{\kappa_e}c_1$ and $A_+=\sqrt{\kappa_e}c_2$. For the case of zero optical and microwave detuning ($\Delta=0$ and $\delta=0$), the pump component A_0 becomes $\alpha_{\rm in}[1+\kappa_e/(-\frac{\kappa}{2}+\frac{\frac{\alpha^2}{4}}{\frac{\kappa}{2}})]$, which indicates that the coherent coupling Ω introduces an effective

which indicates that the coherent coupling Ω introduces an effective intrinsic loss channel for mode c_1 as expected. The total loss for mode c_1 can be written as $\kappa_{1_{\text{eff}}} = \kappa (1 + \left(\frac{\Omega}{\kappa}\right)^2)$ where the factor Ω^2/κ^2 corresponds to the loss rate that is induced by coupling to another mode and plays a similar role as the Purcell effect in cavity quantum electrodynamics. This effective loss balances the large external loss channel (κ_e) to the waveguide and leads to the complete suppression of the pump. Considering the case $\kappa_e \gg \kappa_{\text{intr}}$, we obtain a simple condition for generating a complete frequency shift: $\kappa_e = \Omega^2/\kappa_e$, which means $\Omega = \kappa_e$ when the intrinsic loss is negligible (as is the case for our device).

The concept of balancing the coupling rates can be intuitively understood using impedance matching. For example, when an optical cavity with an intrinsic loss rate $\kappa_{\rm int}$ is coupled to a waveguide with a coupling strength $\kappa_{\rm e}$, some of the light is coupled back to the waveguide. This is identical to the microwave reflection coefficient in transmission-line theory with effective reflection coefficient $\Gamma = (\kappa_{\rm int} - \kappa_{\rm e})/(\kappa_{\rm int} + \kappa_{\rm e})$. In this picture, the case of strong under-coupling $(\kappa_{\rm int} \gg \kappa_{\rm e})$ and over-coupling $(\kappa_{\rm int} \ll \kappa_{\rm e})$ between a waveguide and a cavity corresponds to open and short circuits, respectively. This interpretation helps to understand the cascaded frequency shifting scheme that is discussed in Fig. 4, in which photons propagate through a ladder of energy levels without reflection to realize complete frequency shifts of >100 GHz.

Moreover, the current microwave bandwidth of our two-resonator devices are at least 3 GHz, benefitting from the strong over-coupling of the S and AS modes (linewidths $\sim 2\pi \times 3$ GHz) to the waveguide. We note that the microwave frequency can exceed the linewidth of the S and AS modes owing to the power broadening of the modes by the strong coherent coupling Ω . This effect could be understood by considering the total loss rate $\kappa_{1_{\rm eff}} = \kappa \left(1 + \left(\frac{\Omega}{\kappa}\right)^2\right)$ of mode c_1 , in which the strong Ω leads to a larger loss rate of c_1 thus a broader effective linewidth. A similar analysis can be performed on the AS mode c_2 .

Note that our two-resonator devices can operate without a typical conversion efficiency-bandwidth trade-off. For example, a tenfold reduction in the resonator loss rate (that is an increase in the intrinsic O) will lead to a nearly a tenfold decrease in the on-chip loss α (and a corresponding tenfold increase in efficiency n). This, however, has minimal impact on the device bandwidth, which is dominated by a waveguide-cavity coupling rate y (already up to 31 times larger than intrinsic loss rate). In fact, increasing y not only leads to larger bandwidth, but also further reduces the on-chip loss α and efficiency η . Both effects benefit from the strongly over-coupled regime that our device operates in. Nonetheless, there is a limit to which v can be increased, when parasitic sidebands start overlapping with broadened cavity resonance and thus negatively impact the shift ratio ϵ . This can be avoided by increasing the doublet splitting (see Methods section 'Limitation of the shift ratio of the two-resonator devices'). For example, in the current devices, the shift ratio ϵ is limited by finite suppression of the two parasitic sidebands >25 dB (Fig. 2b, c, insets).

Theoretical expressions of microwave power, coupling rates and on-chip loss for the two-resonator devices

Microwave power and coupling rate \Omega. When the intrinsic loss is non-zero, the GCC condition is $\kappa_{\rm e} = \kappa_{\rm int} + \frac{\Omega^2}{\kappa}$ with $\kappa = \kappa_{\rm e} + \kappa_{\rm int}$, corresponding a coupling rate $\Omega = \sqrt{\kappa_{\rm e}^2 - \kappa_{\rm int}^2}$ to achieve the GCC condition. Thus, the required microwave driving power is

$$\begin{split} P_0 &= \frac{1}{R} \left(\frac{V_0}{\sqrt{2}} \right)^2 = \frac{1}{2} \frac{1}{R} \left(\frac{V_C}{k_{\rm RC}} \right)^2 = \frac{1}{2} \frac{1}{R} \left(\frac{\Omega}{k_{\rm RC} G_V} \right)^2 \\ &= \frac{1}{2} \frac{1}{R} \left(\frac{1}{k_{\rm RC} G_V} \right)^2 (\kappa_{\rm e}^2 - \kappa_{\rm int}^2), \end{split}$$

where V_0 is the peak voltage at the $50-\Omega$ probe, R is the resistance of the probe, V_C is the voltage on the capacitor, $k_{\rm RC} = V_C/V_0$ is determined by the RC limit of the electrode and is frequency-dependent, $G_V = 0.5~{\rm GHz~V^{-1}}$ is the electro-optic coefficient of the device.

Since $\kappa_{\rm e} = \gamma/2$, decreasing the waveguide–cavity coupling rate γ can reduce the required microwave power for efficient frequency shifting (that is, to reach the critical coupling condition). Higher microwave powers are required for increased microwave frequency $\omega_{\rm m}$ because $k_{\rm RC}$ will simultaneously decrease owing to the RC limit of the electrode (discussed in Methods section 'Limitation of the shift frequency of the two-resonator devices').

On-chip loss a. The power of the output signal $a_{\text{out}} = A_0 e^{-i\omega_L t} + A_+ e^{-i\omega_L t} e^{-i\omega_R t}$ is determined by A_0 and A_+ . So the on-chip loss is

$$\alpha = |A_0|^2 + |A_+|^2 = \left(\frac{\kappa_{\text{int}} + \frac{\Omega^2}{\kappa} - \kappa_{\text{e}}}{\kappa_{\text{int}} + \frac{\Omega^2}{\kappa} + \kappa_{\text{e}}}\right)^2 + \frac{4\Omega^2 \kappa_{\text{e}}^2}{(\kappa^2 + \Omega^2)^2},$$

where we use the fact that we are measuring the average power, therefore the interference term of the output signal vanishes. When the GCC condition is achieved, A_0 will vanish. Therefore, the on-chip loss is purely given by the value of A_* :

$$\alpha = |A_+|^2 = \frac{4\Omega^2 \kappa_e^2}{(\kappa^2 + \Omega^2)^2} = \frac{4(\kappa_e^2 - \kappa_{\text{int}}^2)\kappa_e^2}{(\kappa^2 + \kappa_e^2 - \kappa_{\text{int}}^2)^2},$$

where we set $\alpha_{\rm in}=1$ and we use $\Omega=\sqrt{\kappa_e^2-\kappa_{\rm int}^2}$ at the GCC condition. Importantly, it can be seen that the α does not depend on the doublet splitting $2|\mu|$, which determines the shift frequency, and is only determined by the ratio $\frac{\kappa_e}{\kappa_{\rm int}}=\frac{\gamma/2}{\kappa_{\rm int}}$. The device will become lossless ($\alpha=0$) when $\kappa_{\rm int}\to0$.

Unitary transformation of the frequency beam splitter

Here we show that a frequency beam splitter acts on discrete frequency modes according to the same unitary transformation that a beam splitter obeys when acting on spatial modes (paths). Considering a two-resonator device and the case where $\kappa_{\rm int} \rightarrow 0$, that is, that with vanishing on-chip loss, pumping of the S mode with $\Delta = 0$ and $\delta = 0$ gives

$$A_0 = \frac{\Omega^2 - \kappa_e^2}{\Omega^2 + \kappa_e^2},$$

$$A_{+} = ie^{-i\varphi} \frac{2\Omega \kappa_{e}}{\Omega^{2} + \kappa_{e}^{2}},$$

where A_0 and A_+ are the two frequency components of the previously discussed output field $a_{\text{out}} = A_0 \, \mathrm{e}^{-\mathrm{i}\omega_L t} + A_+ \mathrm{e}^{-\mathrm{i}\omega_L t} \mathrm{e}^{-\mathrm{i}\omega_m t}$ and are normalized by the input field α_{in} , alternatively $\alpha_{\text{in}} = 1$. On the basis of this result, we set $A_0 = \cos\theta$ and $A_+ = \mathrm{i}\mathrm{e}^{-\mathrm{i}\varphi}\sin\theta$ with $\theta = \theta(\Omega)$. Similar results in the case of pumping the AS mode can be obtained. Finally, the operator of our frequency splitter is expressed as:

$$U = \begin{pmatrix} \cos \theta(\Omega) & i e^{-i\varphi} \sin \theta(\Omega) \\ i e^{i\varphi} \sin \theta(\Omega) & \cos \theta(\Omega) \end{pmatrix},$$

where the splitting ratio is controlled by Ω , which is governed by the microwave power, while the phase is tuned by the microwave phase φ . We note that our electro-optic device is coherent and does not change other degrees of freedom (for example, polarization or spatial modes) or introduce noise photons from the microwave drive, which is of importance for quantum optics and information tasks (for example, quantum communication and computing). Note that similar arguments apply to the three-resonator cascaded shifter.

Optical parameters of the two-resonator devices

The optical parameters of the two-resonator devices are characterized by sweeping the laser wavelength from 1,580 nm to 1,680 nm and measuring the transmission spectra of the devices. Four parameters are extracted for each device: waveguide–cavity coupling γ , intrinsic loss rate $\kappa_{\rm int}$ of the S and AS modes, linewidth $\kappa = \frac{\gamma}{2} + \kappa_{\rm int}$ of the S and AS modes, and intrinsic quality factor $Q_{\rm intrinsic}$ of the S and AS modes.

For the device with 12.5-GHz doublet splitting, we calculate $\gamma=2\pi\times4.72$ GHz, $\kappa_{\rm int}=2\pi\times0.24$ GHz, $\kappa=2\pi\times2.60$ GHz and $Q_{\rm intrinsic}=0.8\times10^6$ for the doublet at 1,601.3 nm. For the 11.0-GHz device, we selected the resonances at 1,631.5 nm and calculate $\gamma=2\pi\times6.00$ GHz, $\kappa_{\rm int}=2\pi\times0.39$ GHz, $\kappa=2\pi\times3.39$ GHz and $Q_{\rm intrinsic}=0.5\times10^6$. For the 28.2-GHz shift device, we analyse the resonances at 1,633.2 nm and obtain $\gamma=2\pi\times5.31$ GHz, $\kappa_{\rm int}=2\pi\times0.17$ GHz, $\kappa=2\pi\times2.82$ GHz and $Q_{\rm intrinsic}=1.1\times10^6$.

Microwave driving power of the two-resonator device

The microwave driving power is measured by combining the power of the source with the total gain of the electric circuit (including cable losses). The microwave driving powers to achieve the largest shift ratio ε for the two-resonator devices with 12.5-GHz, 11.0-GHz and 28.2-GHz doublet splitting are 102 mW (20.1 dBm), 288 mW (24.6 dBm), and 316 mW (25 dBm), respectively. This corresponds to peak voltages of 3.2 V, 5.4 V and 5.6 V on the 50- Ω probe, respectively. The source power used for those three devices are 0.8 dBm, 0 dBm and –23 dBm with net gains of 19.3 dB, 24.6 dB and 48 dB, respectively.

Using the expressions of microwave power outlined in the previous section, the calculated microwave driving powers are 77 mW, 280 mW and 188 mW for devices with 12.5-GHz, 11.0-GHz and 28.2-GHz doublet splitting, corresponding to peak voltages of 2.8 V, 5.3 V and 4.3 V on the 50- Ω probe, respectively. The $k_{\rm RC}$ for the electrode of each device at their operation frequencies are 1.55, 1.63 and 1.72.

Controlling the shift frequency with d.c. voltage applied to two-resonator devices

The shift frequency can be controlled by detuning the optical resonances of each ring comprising a two-resonator device, resulting in a different splitting between two hybrid modes. However, these detuned coupled resonators will experience a reduced coherent coupling Ω (ref. 33). The device with 12.5-GHz doublet splitting (Fig. 2b, c) is used to investigate this phenomenon by measurement and simulation. We find that the device maintains high shift efficiencies even for large detuning (Extended Data Fig. 6). Theory suggests that a shift ratio ϵ > 0.9 is achievable for shift frequencies of more than 20 GHz, while the measurement is limited by the bandwidth of the microwave amplifier used. In simulation and experiment, the two optical resonators are frequency-detuned by $\delta\omega$ from each other by a d.c. voltage, therefore providing a variation of the two-mode splitting $2\sqrt{(\delta\omega)^2 + \mu^2}$ in which μ is the evanescent coupling between the two rings (doublet splitting is $2|\mu|$). For each two-mode splitting, the frequencies of the applied microwave signals are changed to match the two-mode splitting, while the powers of the microwave signals are invariant from the case that the frequencies of two optical resonators are matched (Fig. 2b, c).

$Characterization \, and \, limitation \, of \, on\text{-}chip \, loss \, for \, two\text{-}resonator \, devices \,$

The on-chip loss for the devices that have doublet splitting of 12.5 GHz, 11.0 GHz and 28.2 GHz are measured to be 0.92 dB, 1.25 dB and 0.45 dB, respectively. The on-chip loss α is defined to be the loss of light that travels through a device. Since our device is resonance-based, light will not go through the device if the laser is far detuned from resonance. Therefore, α is determined by comparing the transmission when the laser is tuned on and far off resonance. The main source of error is the Fabry–Perot fringes that are induced by the two facets of the chip. These fringes produce a variation of the off-resonance transmission. We address this uncertainty by averaging multiple off-resonance powers measured at different wavelengths.

To study the ultimate limit of the on-chip loss, we theoretically calculate α as a function of $Q_{\text{intrinsic}}$ (Extended Data Fig. 7a) with different waveguide–ring coupling rates γ . Since our two-resonator devices operates in the strongly over-coupled regime (loaded quality factor $Q_{\text{load}} \approx 80,000$ for S and AS modes), light only takes a few roundtrips inside the cavity with small propagation losses. As a result, the on-chip loss is close to that of a short bare waveguide. Thus increasing the ratio between waveguide–ring coupling rate γ and the intrinsic loss rate κ_{int} can reduce the on-chip loss, as shown by Extended Data Fig. 7a. For example, increasing $Q_{\text{intrinsic}}$ to 10^7 (ref. 28) will reduce the on-chip loss to 0.04 dB for $\gamma \approx 2\pi \times 8.6$ GHz.

Moreover, although decreasing γ leads to a larger on-chip loss, the required voltage can be largely reduced. For example, for $Q_{\text{intrinsic}} \approx 10^7$, reducing γ to $2\pi \times 3.5$ GHz gives $\alpha = 0.1$ dB and requires only 2 V microwave peak voltage for a frequency shift of 28.2 GHz. Further reducing γ to $2\pi \times 1.7$ GHz yields $\alpha = 0.2$ dB and requires only 1 V microwave peak voltage. (See Methods section 'Limitation of the shift frequency of the two-resonator devices'.)

Limitation of the shift ratio of the two-resonator devices

The shift ratio ϵ in this work is currently limited by the parasitic sidebands of the pump and shifted frequencies (for example, Extended Data Fig. 7b for a two-resonator device). Such parasitic sidebands originate from the Lorentzian shape of the over-coupled hybrid modes. For example, for the two-resonator device with 12.5-GHz doublet splitting (Fig. 2b, c), one of the parasitic sidebands is at a frequency detuning of 25 GHz whereas the other is at -12.5 GHz detuning. This 25-GHz sideband detuning is five times larger than the resonance linewidth. The generation of the two parasitic sidebands can be further suppressed

by increasing the shift frequency or reducing the waveguide–cavity coupling rate γ . A theoretical simulation (Extended Data Fig. 7b) is performed to investigate the power of the parasitic sidebands with varied shift frequency for different waveguide–cavity coupling rates γ . The results show that waveguide–cavity coupling rates up to $2\pi \times 7$ GHz can still ensure sideband power suppression of at least 20 dB below that of the shifted light for a range of shift frequencies >10 GHz and below 30 dB for a range that is >30 GHz. Note that decreasing the waveguide–cavity coupling γ will cause a reduction of the microwave bandwidth. Therefore a proper choice of γ and the shift frequency is required to achieve a high shift ratio and large bandwidth simultaneously. In this work, a 25-dB suppression of the parasitic sidebands below that of the shifted light with a microwave bandwidth of several GHz is achieved in two-resonator devices for shift frequencies of 10–30 GHz.

Limitation of the shift frequency of the two-resonator devices

This limit is due to the electrical circuit and not the optical components. In the main text we showed that the conversion efficiency, carrier suppression ratio, on-chip loss and the shift ratio of each of the two-resonator devices are independent of the shift frequency. To increase the shift frequency, a smaller coupling gap between the two cavities can be used to increase the doublet splitting. Since each of the resonators have a free spectral range of 250 GHz, it is not restricting the doublet splittings of our current device. Also, the intrinsic loss $\kappa_{\rm int}$ and waveguide—ring coupling γ can be maintained when the doublet splitting is increased. However, the electrode performance will degrade at high microwave frequencies. The current electrode is designed to be a capacitor to induce an electric field across the lithium niobate cavity. The impedance of the capacitor decreases with increasing microwave frequency. Thus, the circuit ultimately becomes a short load instead of an open load at high frequencies, and the voltage delivered to the device is reduced.

To quantitatively estimate this frequency limitation from the electrode, we simulate the electrodes shown in Fig. 2a and obtain a 0.11-pF capacitance with a 0.12-nH inductance and 1.5- Ω resistance. We then use an LCR model to calculate the voltage delivered to the capacitor. Extended Data Fig. 8a shows the voltage $V_{\rm C}$ on the capacitor divided by the voltage V_0 on the 50- Ω input probe as a function of microwave frequency. For example, it is obtained that $V_C = 1.72V_0$ at 28.2 GHz and $V_c = 0.5 V_0$ at 84.0 GHz, indicating a lower voltage delivery from the 50- Ω input probe to the capacitor. To estimate the power required at high frequencies, we note that the required coherent coupling strength is $\Omega \approx$ $2\pi \times 3.73$ GHz to achieve the shift ratio $\epsilon = 0.987$ using the device with 28.2-GHz doublet splitting. Combined with the electro-optic coefficient $(\sim 0.5 \, \text{GHz} \, \text{V}^{-1})^{33}$, this coherent coupling strength Ω corresponds to a required voltage of $V_c = 7.46 \text{ V}$ on the capacitor and $V_0 = 4.34 \text{ V}$ on the 50-Ω input probe. In Extended Data Fig. 8b we plot the microwave input power that is needed from the probe as a function of frequency in order to maintain $V_c = 7.46$ V. It can be seen that the required power becomes dramatically higher (>2 W) above ~84 GHz to compensate for the inefficient capacitive drive. To circumvent this problem, one could either design an electrode with lower capacitance or use a taper between the probe and the electrode which transforms the transmission line impedance to lower values and increases the effective RC frequency limit.

Simulation of cascaded frequency shifting

The numerical simulation is performed based on the equations of motion for the cascaded frequency shift system. They are derived using a similar approach (Heisenberg–Langevin equation) to that discussed above:

$$\dot{a}_q = \left(-\mathrm{i}(\omega_q - \omega_1) - \frac{\kappa_{\mathsf{int}1} + \kappa_e}{2}\right) a_q - \mathrm{i}\mu_1 b_1 \delta_{q,1} - \mathrm{i}\mu_1 b_5 \delta_{q,2} - \sqrt{\kappa_e} \alpha_{\mathsf{in}} \delta_{q,1},$$

$$\begin{split} \dot{b_{j}} &= \left(-\mathrm{i}(\omega_{j} - \omega_{L}) - \frac{\kappa_{\mathrm{int2}} + \kappa_{\mathrm{aux}}}{2} \right) b_{j} - \mathrm{i}\Omega \cos(\omega_{\mathrm{m}} t + \varphi) (b_{j+1} + b_{j-1}) \\ &- \mathrm{i}\mu_{1} a_{1} \delta_{j,1} - \mathrm{i}\mu_{1} a_{2} \delta_{j,5} - \mathrm{i}\mu_{2} c_{1} \delta_{j,0} - \mathrm{i}\mu_{2} c_{2} \delta_{j,6}, \end{split}$$

$$\dot{c}_p = \left(-\mathrm{i}(\omega_p - \omega_\mathrm{L}) - \frac{\kappa_{\mathrm{int3}}}{2}\right)c_p - \mathrm{i}\mu_2 b_0 \delta_{p,1} - \mathrm{i}\mu_2 b_6 \delta_{p,2},$$

where a_q , b_j , c_p represent the annihilation operators of modes in rings 1, 2, 3, respectively (q=1,2;j=0,1,2,3,4,5,6;p=1,2). In ring 2, the modes b_1 , ..., b_5 correspond to modes 1 to 5 in Fig. 4b. In ring 1, a_1 and a_2 are the input and output modes that couple to b_1 and b_5 , respectively. In ring 3, c_1 and c_2 are the modes that couple to b_0 and b_6 , which creates boundaries for the cascaded process. The Kronecker delta $\delta_{i,j}$ gives 1 when i=j and 0 when $i\neq j$. The effective intrinsic loss rate κ_{aux} for ring 2 is induced by the coupling to the auxiliary waveguide (Fig. 4c) while κ_{int1} , κ_{int2} and κ_{int3} represent the intrinsic loss rate of rings 1, 2 and 3, respectively. The simulations are performed using similar methods described in Methods section 'Numerical simulation of the two-resonator device'.

For the simulations, we assume all three cavities to have an intrinsic $Q \approx 1.8 \times 10^6$, which corresponds to an intrinsic loss rate $\kappa_{\rm int} = 2\pi \times 100$ MHz. The waveguide–mode coupling of ring 1 is $\kappa_{\rm e} = 2\pi \times 3$ GHz, the ring 1–ring 2 evanescent coupling is $\mu_1 = 2\pi \times 1.5$ GHz, and the ring 2–ring 3 coupling is $\mu_2 = 2\pi \times 3$ GHz. The coupling induced by microwave modulation is $\Omega = 2\pi \times 3$ GHz, which is similar to that used in our current devices.

Extended Data Fig. 9a shows that the simulated shift ratio ϵ can reach near unity with a 1.1-dB on-chip loss for a 120-GHz shift using a single and continuous 30-GHz microwave drive. Larger frequency shifts $(n-1)\omega_{\rm m}$ can be realized by increasing the number of modes n without compromising the high shift ratio, at a cost of an added on-chip loss of 0.15 dB per mode (Extended Data Fig. 9b).

Device parameters of the cascaded frequency shifter

The device parameters of the cascaded frequency shifter are extracted from the transmission spectrum of the device, as measured using the bus and auxiliary waveguide. The parameters are summarized in Extended Data Table 2. The shift ratio ϵ and on-chip loss α are mainly limited by the mismatch of the FSRs of ring 1 ($2\pi \times 123.9$ GHz) and ring 2 $(2\pi \times 29.825 \, \text{GHz})$. This mismatch originates from the strong evanescent coupling, μ_1 and μ_2 , which distorts the FSR of ring 2 through a non-resonant perturbation. For example, whereas μ_2 provides a strong boundary by forming a doublet splitting through the coupling of modes c_1 and b_0 (Fig. 4b), mode c_1 also couples to b_1 off-resonantly and leads to a frequency changes of mode b_1 of the order of approximately μ_2^2 /FSR_{original,2} $\approx 2\pi \times 1.5$ GHz (second-order perturbation theory), where $FSR_{original,2} \approx 2\pi \times 30.925$ GHz is the designed FSR of ring 2 without coupling to other rings. Reducing the coupling strength of μ_1 and μ_2 to $\sim 2\pi \times 1$ GHz will enable matching of the FSRs to satisfy the GCC condition without affecting the boundary. Finally, the FSR of ring 3 is not precisely extracted given that there is not an auxiliary waveguide on ring 3. However, this parameter does not affect the cascaded process because ring 3 is used only to break the cascade.

Data availability

The datasets generated and analysed during the current study are available from the corresponding author on reasonable request.

 Wang, C. et al. Monolithic lithium niobate photonic circuits for Kerr frequency comb generation and modulation. Nat. Commun. 10, 978 (2019).

Acknowledgements We thank C. Wang, C. Reimer, J. Lukens and P. Lougovski for helpful discussions. This work is supported by the US Office of Naval Research (QOMAND N000014-15-1-2761), Air Force Office of Scientific Research (FA9550-19-1-0310 and FA9550-20-1-0105), National Science Foundation (ECCS-1839197, ECCS-1541959 and PFI-TT IIP-1827720), Army Research Office (W911NF2010248), and Department of Energy (HEADS-QON DE-SC0020376). Device fabrication was performed at the Harvard University Center for Nanoscale Systems. D.Z. acknowledges support by the Harvard Quantum Initiative post-doctoral fellowship. N.S. acknowledges support by the Natural Sciences and Engineering Research Council of Canada (NSERC) and the AQT Intelligent Quantum Networks and Technologies (INQNET) research programme. E.P. acknowledges support by a Draper Fellowship.

Author contributions Y.H. and M.Z. conceived the idea. Y.H. developed the theory, performed numerical simulations and fabricated the devices. Y.H., M.Y. and D.Z. carried out the measurements with N.S. assisting. Y.H., N.S., D.Z., M.Y., M.Z. and M.L. wrote the manuscript. A.S.-A., L.S., J.H. and E.P. helped with the project. M.L. supervised the project.

Competing interests M.Z. and M.L. are involved in developing lithium niobate technologies at HyperLight Corporation.

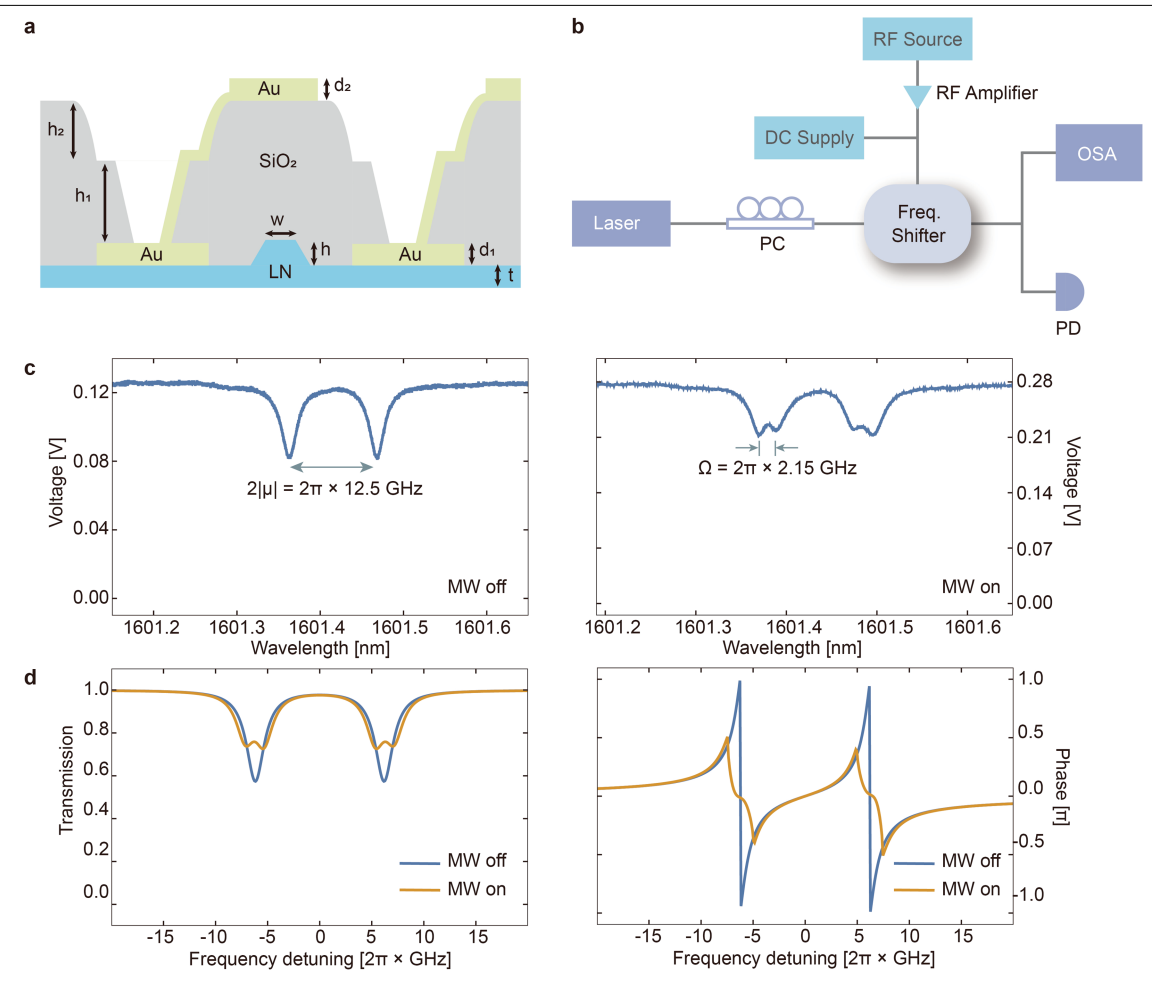
Additional information

 $\textbf{Supplementary information} \ The \ online \ version \ contains \ supplementary \ material \ available \ at \ https://doi.org/10.1038/s41586-021-03999-x.$

Correspondence and requests for materials should be addressed to Marko Lončar.

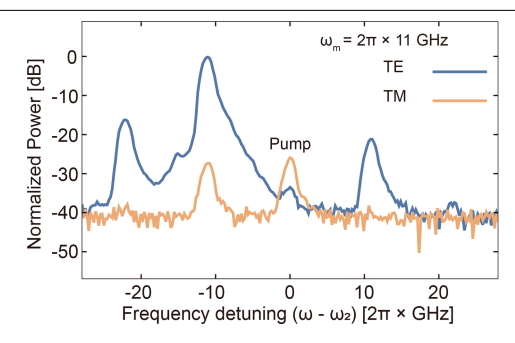
Peer review information Nature thanks Andrew Weiner and the other, anonymous, reviewer(s) for their contribution to the peer review of this work. Peer reviewer reports are available.

Reprints and permissions information is available at http://www.nature.com/reprints.

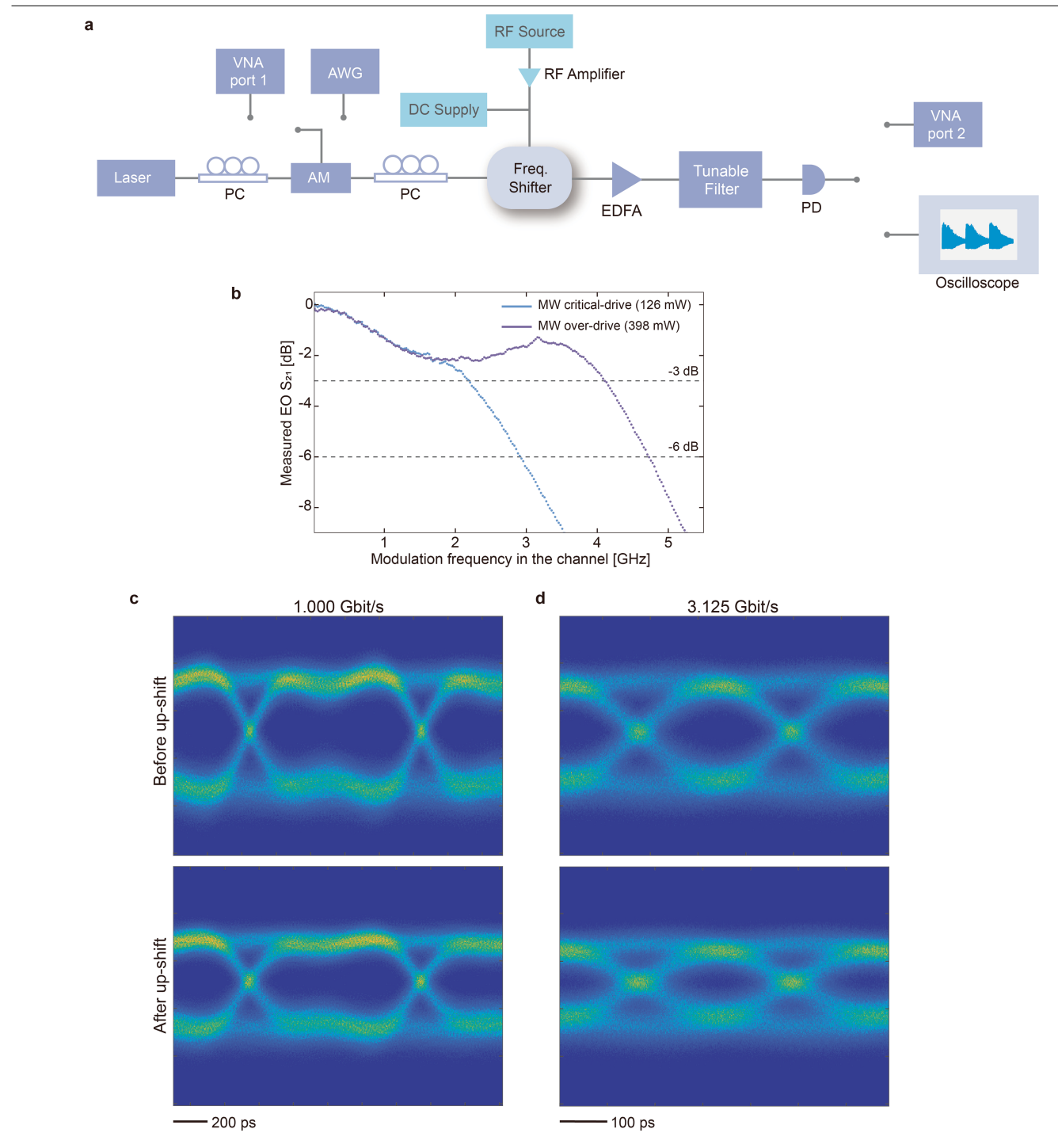


Extended Data Fig. 1 | Illustration of the cross-section of one of the two-resonator devices, set-up of frequency shift measurements, and optical transmission spectra. a, Cross-section of one of the two-resonator devices. The parameters labelled in the cross-section are $w=1.2~\mu m, h=350~nm, t=250~nm, d_1=300~nm, d_2=500~nm,$ and $h_1=h_2=800~nm$. b, Set-up for measuring frequency up- and down-shifts. PC, polarization controller; OSA,

optical spectrum analyser; PD, photodetector. \mathbf{c} , Measured transmission spectrum of the 12.5-GHz two-resonator device (Fig. 2b, c) when the microwave drive is turned off (left panel) and on (right panel). \mathbf{d} , Simulation of the transmission and phase spectra of the 12.5-GHz two-resonator device in the presence and absence of the microwave drive. MW, microwave.

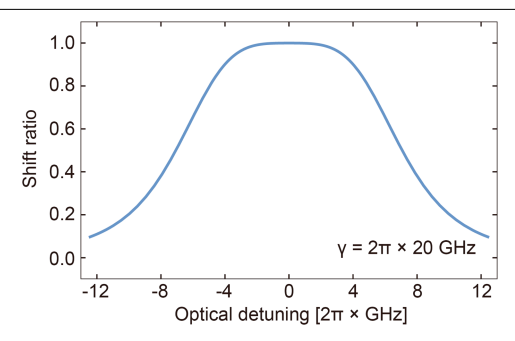


 $\label{lem:extended} \textbf{Data Fig. 2} | \textbf{Polarization of the frequency shifter output.} This measurement is performed on a two-resonator device with 11.0 GHz doublet splitting. The TE and TM components of the output light are measured using an optical spectrum analyser after passing a polarizer. Here the power is normalized by the summation of TE and TM output powers.$

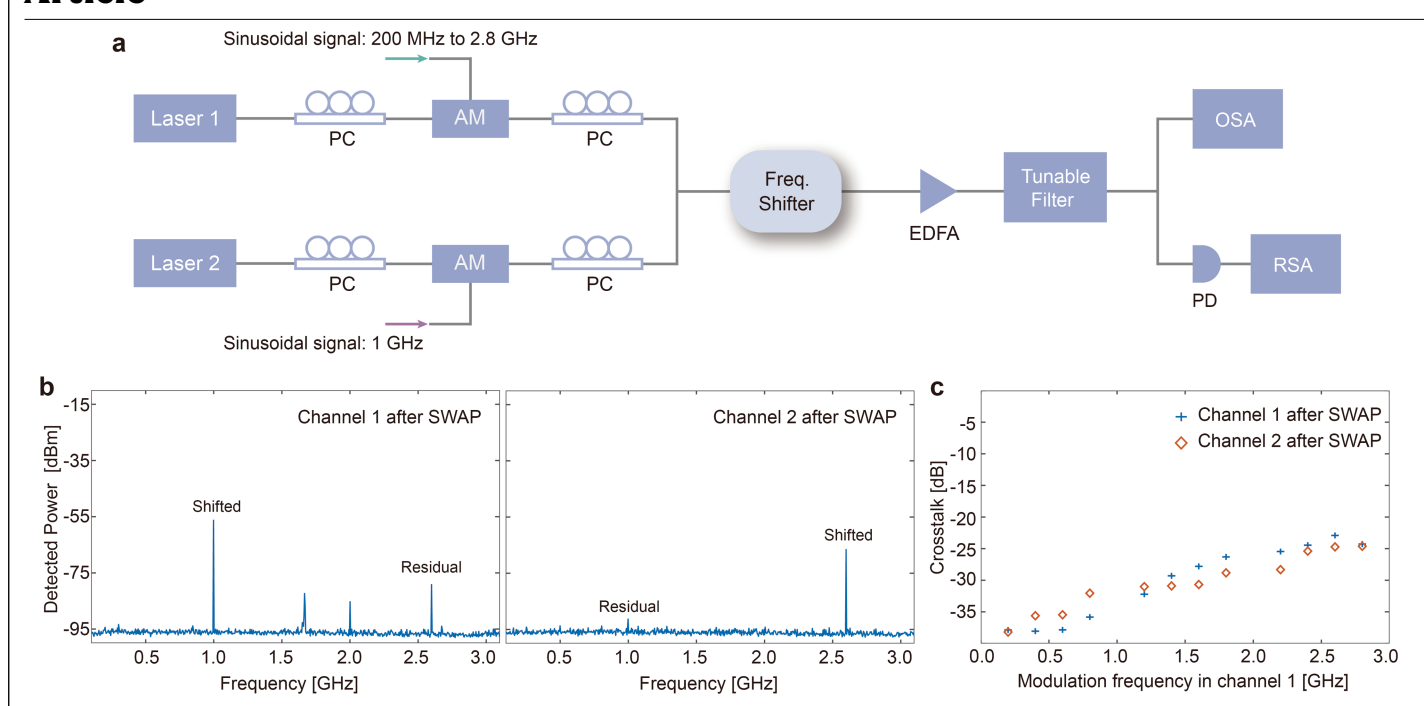


Extended Data Fig. 3 | Modulation bandwidth and frequency channel shifting with pseudorandom bit sequences. a, Experimental set-ups. The input laser beam is modulated by either a sinusoidal signal from the port 1 of a vector network analyser (VNA) (bandwidth measurement) or an actual data stream that is generated by an arbitrary waveform generator (AWG) (eye diagram measurement). The input light is up-shifted and detected by a photodetector (PD) followed by either port 2 of the VNA (bandwidth measurement) or an oscilloscope (eye diagram measurement). The measurements are performed at a wavelength of 1,560 nm on the two-resonator device in Fig. 2b, c, in which the doublet splitting is 11.3 GHz due

to optical dispersion (doublet splitting is $12.5\,\mathrm{GHz}$ at $1,601\,\mathrm{nm}$). **b**, Measured modulation bandwidth of the device. The 3-dB modulation bandwidth is $2.2\,\mathrm{GHz}$, corresponding to an optical bandwidth of $4.4\,\mathrm{GHz}$. The modulation bandwidth is broadened to $4.1\,\mathrm{GHz}$ by increasing the microwave driving power from $126\,\mathrm{mW}$ to $398\,\mathrm{mW}$. **c**, Measured eye diagrams when using actual data streams to modulate the input laser beam. The eye diagrams before shift are measured by setting the input laser beam off-resonance with the filter window centered to the input wavelength (filter bandwidth unchanged). By comparing the amplitude of the eye diagrams before and after swap, we found the loss is $-1\,\mathrm{dB}$ which is consistent with the on-chip loss (0.92 dB).



Extended Data Fig. 4 | **Simulated shift ratio as a function of the detuning of the laser.** The simulated two-resonator device is optimized for high optical bandwidth. Design parameters: $\gamma=2\pi\times20\,$ GHz (leads to a $\kappa_e=2\pi\times10\,$ GHz), $\kappa_{\rm int}=2\pi\times170\,$ MHz, $\omega_m=2\pi\times28.2\,$ GHz. A 3-dB optical bandwidth of -14 GHz can be achieved using a critical-drive microwave power of 1.35 W with a 26.7 dB suppression of parasitic sidebands and 0.13 dB on-chip loss. The microwave power for a 50–50 split on such a device is expected to be 238 mW.

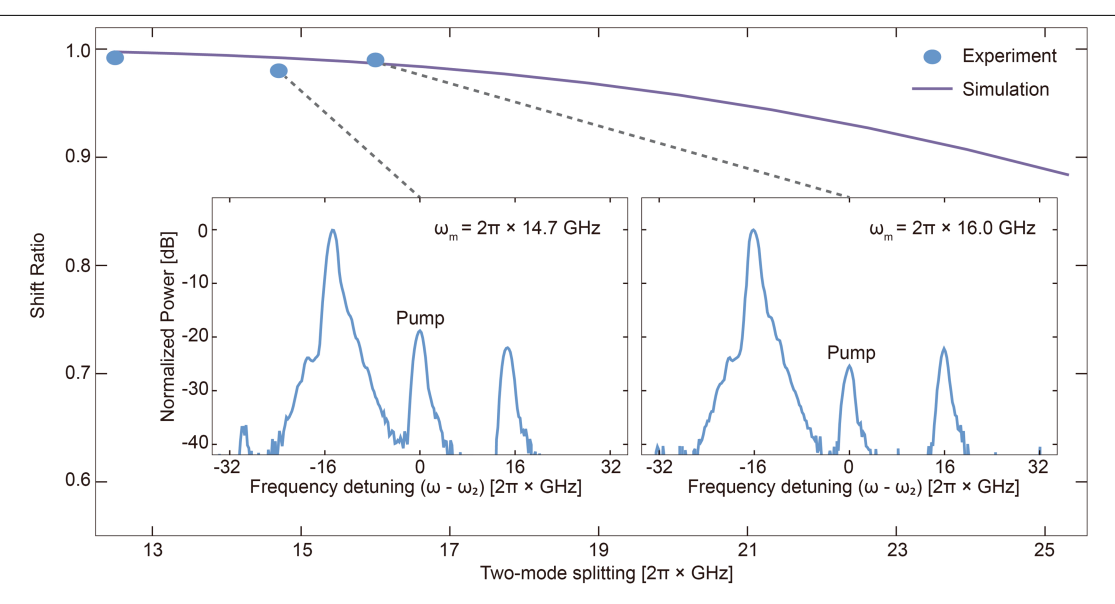


Extended Data Fig. 5 | Crosstalk measurement for channel swapping.

 $\label{eq:apper} \textbf{a}, Experimental set-ups for the crosstalk measurement. Two input laser beams are each independently modulated by a sinusoidal signal to define two distinct frequency channels, sent into a two-resonator device, and detected by an OSA and a PD followed by an RSA. The sinusoidal signal applied to the input beam of channel 1 (matching the S resonance) is swept from 200 MHz to 2.8 GHz while the sinusoidal signal on the input beam of channel 2 (matching the AS resonance) is kept at 1 GHz. Each channel is selected by a tunable filter.$

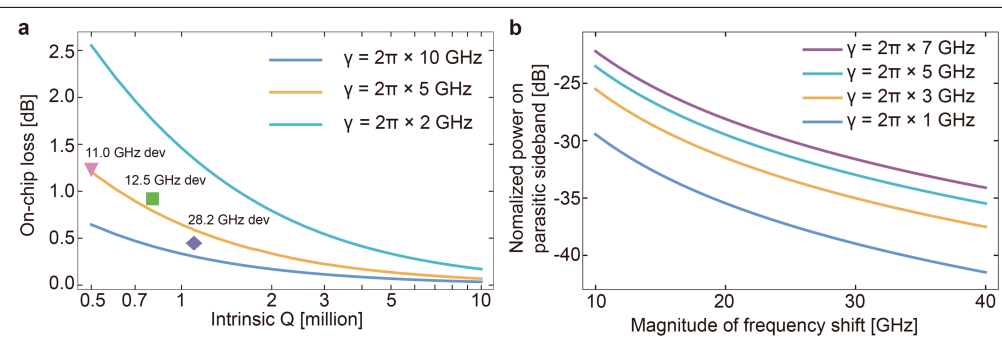
 \mathbf{b} , Radio-frequency spectrum for channel 1 and channel 2 after the swap when the modulation frequency in channel 1 is set to 2.6 GHz depicts low crosstalk in the swap measurements. The crosstalk is defined as the ratio between the

shifted frequency and the residual frequency. The frequency component of 1.6 GHz that appears in channel 1 is the beat note between the shifted frequency and the residual frequency. The 2 GHz component is the second harmonic signal that is generated by the amplitude modulator, which is verified beforehand. $\bf c$, Measured crosstalk for two channels when sweeping the modulation frequency in channel 1 from 200 MHz to 2.8 GHz. We find the crosstalk to be approximately -35 dB at low frequency (several hundreds of MHz) and approximately -25 dB at 2.8 GHz. PC, polarization controller; AM, amplitude modulator, EDFA, erbium-doped fibre amplifier; OSA, optical spectrum analyser; PD, photodetector; RSA, real-time spectrum analyser.



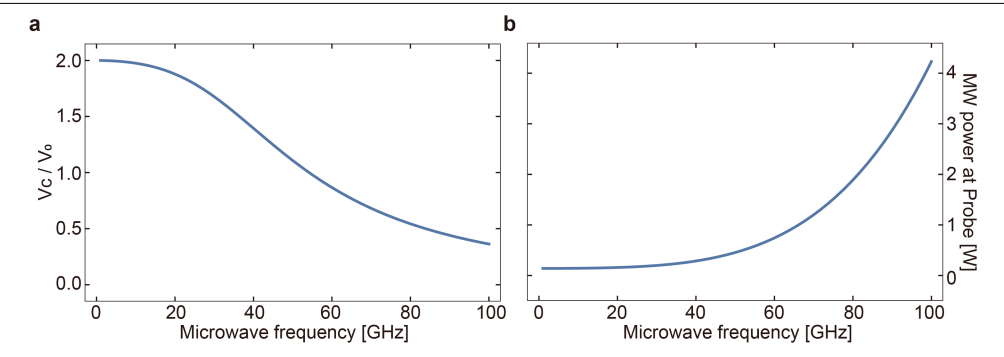
 $\label{lem:extended} \textbf{Extended Data Fig. 6} \ | \ \textbf{Varying the shift frequency with d.c. voltage.} \ Each \ of the resonators in a 12.5-GHz two-resonator device (Fig. 2b, c) are detuned from each other using a d.c. voltage to provide a variation of the frequency difference between the two hybrid modes. For each frequency difference$

between two modes, the microwave frequency is changed to match this difference, while the powers of the microwave signals are kept constant and equal to that used when the resonances of each ring are degenerate (Fig. 2b, c). The shift ratio remains >0.9 when the shift frequency is detuned >20 GHz.



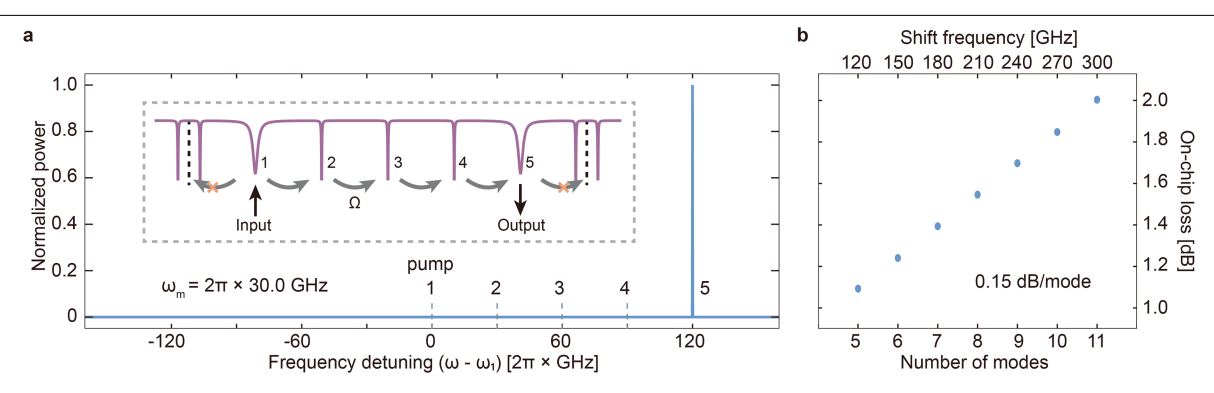
Extended Data Fig. 7 | **Limitation of the on-chip loss and parasitic sidebands. a**, Predicted two-resonator on-chip loss with varied $Q_{\rm intrinsic}$ for different waveguide-ring couplings γ . The theoretical curve of on-chip loss is calculated under the optimal condition of both pump and microwave detunings are zero. The measured on-chip loss of the 11.0 GHz, 12.5 GHz and 28.2 GHz devices used in this work are labelled with a triangle, square, and diamond, respectively. **b**, Simulation of the normalized power of the parasitic

sidebands as a function of the shift frequency. The waveguide–cavity coupling rate γ is varied from $2\pi \times 1$ GHz to $2\pi \times 7$ GHz. Waveguide–cavity coupling rates that are as high as $2\pi \times 7$ GHz can still keep the parasitic sidebands suppressed below 20 dB for shift frequencies>10 GHz and below 30 dB for shifts that are >30 GHz. In this work, the parasitic sidebands are lower than 25 dB in devices at shift frequencies of 10-30 GHz.



Extended Data Fig. 8 | Simulated electrode performance for varied microwave frequencies. a, The relative voltage delivered to the capacitor $V_{\rm C}$ and probe $V_{\rm O}$ for varied microwave frequencies. b, Power required at the probe (50 Ω) for a maximal shift ratio as a function of microwave frequency. Our current 28.2 GHz two-resonator device requires 188 mW of theoretical

microwave power (4.34 V microwave peak voltage). We assume that the voltage $V_{\rm C}$ delivered to the capacitor is kept identical to the peak-voltage on capacitor ($V_{\rm C}$ = 7.46 V) of our 28.2 GHz device when reaching 0.987 shift ratio. MW, microwave.



$\textbf{Extended Data Fig. 9} \, | \, \textbf{Simulation of the cascaded frequency shifter.} \\$

 $\label{eq:action} \textbf{a}, Simulated optical spectrum shows a cascaded frequency shift when the GCC condition is satisfied. A single microwave tone at 30 GHz (equal to the FSR of ring 2) generates a five-mode cascaded frequency shift of 120 GHz with an$

on-chip loss of 1.1 dB. The inset illustrates the energy flow in the coupled cavities system. The frequency of mode 1 in the x axis of the inset is denoted by ω_1 . **b**, The shift can be scaled to a larger number of modes, with an incremental on-chip loss of 0.15 dB per mode.

Extended Data Table 1 | Parameters of the two-resonator devices

Parameters	12.5 GHz device	11.0 GHz device	28.2 GHz device
Conversion efficiency η	80%	73%	89%
Carrier suppression ratio CSR	33 dB	23 dB	20 dB
Shift ratio ϵ	0.993	0.977	0.987
On-chip loss α	0.92 dB	1.25 dB	0.45 dB
Microwave Power for full conversion	102 mW	288 mW	316 mW
Mode linewidth κ	$2\pi \times 2.60~\mathrm{GHz}$	$2\pi \times 3.39 \text{ GHz}$	$2\pi \times 2.82~\mathrm{GHz}$
Intrinsic loss rate κ_{int}	$2\pi \times 0.24~\mathrm{GHz}$	$2\pi \times 0.39~\mathrm{GHz}$	$2\pi \times 0.17~\mathrm{GHz}$
Intrinsic quality factor $Q_{ m intrinsic}$	0.8×10^6	0.5×10^6	1.1×10^6
Waveguide-cavity coupling rate γ	$2\pi \times 4.72~\mathrm{GHz}$	$2\pi \times 6.00 \text{ GHz}$	$2\pi \times 5.31~\mathrm{GHz}$

Extended Data Table 2 | Parameters of the cascaded frequency shifter

Parameters	Cascaded frequency shifter	
Conversion efficiency η	19%	
Carrier suppression ratio CSR	10 dB	
Shift ratio ϵ	0.809	
On-chip loss $lpha$	6.17 dB	
Microwave power	550 mW	
External coupling to bus waveguide of Ring 1 κ_e	$2\pi \times 2.20 \text{ GHz}$	
Coupling rate between Ring 1 and Ring 2 μ_1	$2\pi \times 2.49 \text{ GHz}$	
Coupling rate between Ring 2 and Ring 3 μ_2	$2\pi \times 6.86 \mathrm{GHz}$	
Intrinsic loss rate of Ring 1 κ_{int1}	$2\pi \times 0.14~\mathrm{GHz}$	
Intrinsic loss rate of Ring 2 κ_{int2}	$2\pi \times 0.10~\mathrm{GHz}$	
Effective intrinsic loss rate of Ring 2 induced by	$2\pi \times 0.10~\mathrm{GHz}$	
auxiliary waveguide κ_{aux}		
Intrinsic loss rate of Ring 3 κ_{int3}	$2\pi \times 0.17~\mathrm{GHz}$	
Ring 1 FSR	$2\pi \times 123.9 \text{ GHz}$	
Ring 2 FSR	$2\pi \times 29.825 \mathrm{GHz}$	
Ring 3 FSR	$\sim 2\pi \times 180~\mathrm{GHz}$	